

Stage-1 cationic C₆₀ intercalated graphene oxide films

Xianjue Chen,^{1,*} Karin Ching,¹ Aditya Rawal,² Douglas J. Lawes,² Mohammad Tajik,¹ William A. Donald,¹ Sun Hwa Lee,³ and Rodney S. Ruoff^{3,4,5,6,*}

¹ *School of Chemistry, University of New South Wales, Sydney, New South Wales 2052, Australia*

² *Mark Wainwright Analytical Centre, University of New South Wales, Sydney, New South Wales 2052, Australia*

³ *Center for Multidimensional Carbon Materials (CMCM), Institute for Basic Science (IBS), Ulsan 44919, Republic of Korea*

⁴ *Department of Chemistry, Ulsan National Institute of Science and Technology (UNIST), Ulsan 44919, Republic of Korea*

⁵ *School of Materials Science and Engineering, Ulsan National Institute of Science and Technology (UNIST), Ulsan 44919, Republic of Korea*

⁶ *School of Energy and Chemical Engineering, Ulsan National Institute for Science and Technology (UNIST), Ulsan 44919, Republic of Korea*

**Email: correspondence and requests for materials should be addressed to X.C. (xianjue.chen@unsw.edu.au) and R.S.R. (ruofflab@gmail.com)*

Abstract

A “stage-1” intercalated film has been made by the ion exchange of “cationic C₆₀” (pyrrolidinium-functionalised C₆₀, C₆₀(Py)ⁿ⁺) into centimetre-wide, micrometre-thick air-dried graphene oxide (G-O) films composed of tens of thousands of layers of stacked/overlapping G-O platelets, denoted [C₆₀(Py)ⁿ⁺]G-O films. Spontaneous intercalation by ion exchange of one layer of cationic C₆₀ between adjacent G-O layers expands the interlayer spacing of the films from 0.74 nm to 1.46 nm. The films remain intact in water and various organic solvents, which is likely due to a strong affinity between C₆₀(Py)ⁿ⁺ and G-O. Membranes made of the films showed a 6.8 times faster water vapour permeation rate (allowing the vapour to transport through the membrane almost freely) and a 10.5 times faster liquid water permeation rate than G-O membranes. Heating the films at 2000 °C under applied pressure or at 2700 °C without physical confinement converted them into highly graphitised structures.

“Bottom up” assembly of carbon “building blocks” can lead to new structures whose properties can then be explored. Examples of such materials include the “peapod” (an array of C_{60} encapsulated in carbon nanotubes)¹ and the “buckyball sandwich” (one layer of C_{60} confined between two layers of graphene)². In addition, a graphite intercalation compound (GIC) with C_{60} intercalated between adjacent layers has been predicted to be stable³, although it did not form by directly exposing graphite to C_{60} vapour or a solution of C_{60} ⁴. In attempts to intercalate C_{60} , well-known GICs were first formed, followed by their exposure to a C_{60} solution for the possible formation of co-intercalated compounds^{4,5}. Achieving the assembly of different forms of carbon into new long-range ordered structures on a macroscopic scale is important.

Graphene oxide (G-O) is an oxidised form of graphene, typically prepared by the oxidation of graphite flakes to graphite oxide and subsequent exfoliation into single layers⁶. Solid ‘G-O films’ (or ‘papers’) composed of stacked and overlapping layers of G-O platelets have a lamellar structure that can also be densely-packed, and has an interlayer spacing that depends on the amount of intercalated water⁷. G-O films (or graphite oxide particles) can act as a “host” to accommodate intercalants because the interlayer galleries facilitate “guest” species entering and binding to the G-O layers. Oxygen-containing groups on G-O give it a negative charge that is balanced by hydronium ions, yielding an electrical double layer at the water/G-O interface⁸. Ion exchange allows the selective intercalation of organic or inorganic cationic species into G-O films, which causes an increase in interlayer spacing and film thickness depending on the size and orientation(s) of the intercalants⁹⁻¹⁵.

Here, we report the preparation of pyrrolidinium-functionalised C_{60} ($C_{60}(\text{Py})^{n+}$) intercalated G-O films by ion exchange after immersing G-O films into an aqueous $C_{60}(\text{Py})^{n+}$ salt solution, **Fig. 1a** (inset). An air-dried intercalated film

([C₆₀(Py)ⁿ⁺]G-O film) shows an increased interlayer spacing and a “stage-1”-like intercalation of C₆₀(Py)ⁿ⁺ between adjacent G-O layers. The structure, chemical composition, and thermal and chemical stabilities of the film are presented and discussed below. Water permeation through the G-O membranes and the [C₆₀(Py)ⁿ⁺]G-O membranes showed a significantly higher flux for the latter. The thermal decomposition and graphitisation of the film have also been studied as described below.

Results and discussion

G-O films prepared by vacuum-filtering an aqueous G-O dispersion were immersed in a C₆₀(Py)ⁿ⁺ salt solution and collected after soaking for a given time. The resulting film remained intact; the dried film showed a 61% increase in mass compared to the original film. Thin-film X-ray diffraction (XRD) patterns of the G-O film before and after soaking are shown in **Fig. 1a**. The (001) peak shifts from 11.9° for the G-O film to 6.0° for the [C₆₀(Py)ⁿ⁺]G-O film, corresponding to an increase of the mean d-spacing from 0.74 to 1.46 nm. Similar changes in d-spacing were observed from *ex situ* XRD for thinner films after soaking for different durations (**Fig. S2**). In the early stages the (001) peak from the G-O film broadened and shifted slightly to 10°, and then as the soaking time increased a new peak appeared at 6.5°, whose intensity increased and position shifted to a lower 2θ value while the 10° peak gradually disappeared. The position and width of the new peak remained unchanged after soaking for a time that depends on the thickness of the G-O film. Thicker films required a longer time to reach full expansion, e.g. 3 days for a 0.3- μ m thick G-O film (**Fig. S2a**), and 3 weeks for a 2.5- μ m thick film (**Fig. 1a**). The XRD pattern of the C₆₀(Py)ⁿ⁺ salt (**Fig. S3**) has a broad peak at 20°, and a few small sharp peaks. The

absence of all of these peaks in the XRD pattern of the $[C_{60}(Py)^{n+}]G-O$ film indicates the complete removal of the salt (or at least: any crystals of it) by washing after soaking.

The fully expanded $[C_{60}(Py)^{n+}]G-O$ film was nearly twice the mean thickness of the original (e.g., from 2.5 to 4.9 μm) and it retained its compact, layer structure, as shown by scanning electron microscopy (SEM) of the cross-section after fracture, (**Figs. 1b and 1c**). Atomic force microscopy (AFM) topography images of a typical single-layer G-O platelet and a G-O with $C_{60}(Py)^{n+}$ adsorbed on the surface are shown in **Figs. 1d and 1e**, with heights (**Fig. 1f**) of 1.25 nm for G-O and 1.50 nm for $[C_{60}(Py)^{n+}]G-O$. The thickness of G-O is consistent with the previously reported value measured in ambient conditions where its hydrophilic surface has likely adsorbed a thin layer of water¹⁶. Note that the surface of the $[C_{60}(Py)^{n+}]G-O$ film is less hydrophilic than that of the G-O film, (**Fig. 1g**) which may be due to the anchoring of $C_{60}(Py)^{n+}$ on the surface of G-O. Another study has reported that the wetting properties of G-O films are sensitive to cationic modification¹⁷. The $[C_{60}(Py)^{n+}]G-O$ platelet has an average peak-to-valley roughness of 0.81 nm compared to 0.40 nm for G-O, possibly due to the presence of $C_{60}(Py)^{n+}$ on G-O, which might also influence the surface wetting properties of the $[C_{60}(Py)^{n+}]G-O$ film¹⁸.

The expansion of the interlayer spacing is due to a “stage-1”-like intercalation of $C_{60}(Py)^{n+}$, driven by ion exchange of $C_{60}(Py)^{n+}$ with the hydronium ions that were balancing the negatively charged surface of G-O⁸, consistent with the drop of pH from 4.7 to 3.6 for the $C_{60}(Py)^{n+}$ salt solution after soaking. In addition, we find that $C_{60}(Py)^{n+}$ can enter from both the surface and the edge of the G-O films, **Fig. S4**. The $[C_{60}(Py)^{n+}]G-O$ film remained stable while soaking in water and various organic solvents (**Fig. S5**), resistant to further attempted ion exchange with monovalent

cations (**Fig. S6**), and also to “shock cooling” in liquid nitrogen (**Fig. S7**). The structure of the film was, however, sensitive to heating as shown by the loss of the broad XRD (001) peak after heating at 160 °C in air, **Fig. S8**. The (001) peak also disappeared after treatment with hydroiodic acid¹⁹, **Fig. S9**.

Transmission electron microscopy (TEM) was used to examine the possible presence of $C_{60}(Py)^{n+}$ in the $[C_{60}(Py)^{n+}]G-O$ film. A typical high-resolution TEM (HRTEM) image of the $C_{60}(Py)^{n+}$ salt (**Fig. S10**) shows the 0.7-nm ‘nuclear framework’ diameter of C_{60} molecules. We found that imaging $[C_{60}(Py)^{n+}]G-O$ was influenced by the highly defective nature of the G-O. That said, $C_{60}(Py)^{n+}$ with a similar size to that in the pure $C_{60}(Py)^{n+}$ was observed (**Fig. 2a**) with several indicated in the inset magnified image. The $C_{60}(Py)^{n+}$ molecular cations are well-dispersed on the G-O as is evident from the elemental maps (**Fig. 2b**) showing a uniform distribution of N, which is only present in the $C_{60}(Py)^{n+}$, over the G-O.

In an attempt to study the change in interlayer spacing, focused ion beam (FIB) was used to prepare thin lamellae from the films for cross-sectional TEM imaging. The cross-section of a G-O film (**Fig. 2c**) shows a set of lattice fringes parallel to the film surface, indicative of a layer structure. The lattice spacing is about 0.5 nm, based on the fast Fourier transform (FFT) (inset) which is smaller than that obtained from XRD (0.74 nm), which suggests the removal of interlamellar water under ultrahigh vacuum in the TEM or the partial reduction of G-O by FIB sample preparation; we note that films comprised of partially reduced or strongly reduced G-O layers have lower to zero interlamellar water, than G-O films. The diffuse (001) diffraction spots (see FFT image) are indicative of a less ordered structure than, say, graphite, and this is typical for G-O films made of randomly stacked/overlapping platelets⁷. For the $[C_{60}(Py)^{n+}]G-O$ film (**Fig. 2d**), the increased interlayer spacing is

evident from the shift of the diffuse spots towards the centre of the FFT image, but this made its estimation difficult.

Fourier-transform infrared (FTIR) spectra were acquired for the G-O film, the $C_{60}(\text{Py})^{n+}$ salt and the $[C_{60}(\text{Py})^{n+}]$ G-O film (**Fig. 3a**). The representative spectrum of the G-O film shows peaks corresponding to C=C ($1500\text{-}1720\text{ cm}^{-1}$) from pristine sp^2 -hybridised regions, as well as C-O ($1020\text{-}1250\text{ cm}^{-1}$), C=O ($1680\text{-}1780\text{ cm}^{-1}$) and O-H ($2500\text{-}3700\text{ cm}^{-1}$) from various oxygen-containing groups and/or absorbed water²⁰. The spectrum of the $[C_{60}(\text{Py})^{n+}]$ G-O film shows similar features, while peaks assigned to CH_3 ($1350\text{-}1500\text{ cm}^{-1}$) from methyl groups and C-N (967 and 945 cm^{-1}) from pyrrolidinium (**Py**) groups in $C_{60}(\text{Py})^{n+}$ were detected. Of note in the $[C_{60}(\text{Py})^{n+}]$ G-O spectrum is the absence of the peak corresponding to sulfate groups, suggesting the rejection of sulfate ions as the $C_{60}(\text{Py})^{n+}$ was intercalating into G-O films.

The chemical compositions of G-O, the $C_{60}(\text{Py})^{n+}$ salt, and the $[C_{60}(\text{Py})^{n+}]$ G-O film were studied by X-ray photoelectron spectroscopy (XPS) and the full survey spectra are given in **Fig. S11**, which show an increased C/O atomic ratio (from 2.2 to 3.7) and an increased N content (from 0 to 2.56 at.%) upon $C_{60}(\text{Py})^{n+}$ intercalation. In addition, a trace amount of S (0.25 at.%) was detected for the G-O film, possibly from residual covalent sulfates formed during the preparation of the G-O²¹. The S content remained at 0.45 at.% in the $[C_{60}(\text{Py})^{n+}]$ G-O film, suggesting that the sulfate ions (3.50 at.% S) in the $C_{60}(\text{Py})^{n+}$ salt were mostly rejected during the intercalation, consistent with the FTIR analysis. Based on the XPS result, the amounts of C in the $[C_{60}(\text{Py})^{n+}]$ G-O film contributed by G-O and $C_{60}(\text{Py})^{n+}$ are 36.9 at.% and 39.4 at.%, respectively. Similar changes in elemental composition were seen from combustion elemental analysis, where the C content increased from 44.6 to 57.2 wt.% while the O content dropped from 48.3 to 38.8 wt.% after $C_{60}(\text{Py})^{n+}$ intercalation. There was also

an increase of N content from 0 to 1.7 wt.%, while the S content remained nearly unchanged (0.8 wt.% for the G-O and 0.7 wt.% for the $[C_{60}(Py)^{n+}]G-O$ film).

High-resolution XPS C1s and N1s spectra are shown in **Fig. 3b**. The C1s spectrum of G-O could be de-convoluted into three peaks at binding energies of 284.8 eV for C-C and/or C=C, 287.0 eV for C-O (epoxide and/or C-OH groups), and 288.5 eV for C=O (carbonyl groups)²². The spectrum of the $C_{60}(Py)^{n+}$ salt consisted of two peaks centred at 284.5 eV for C-C and/or C=C, and 285.8 eV for C-N. The $[C_{60}(Py)^{n+}]G-O$ film showed the peak for C-C and/or C=C, with a higher relative intensity indicative of $C_{60}(Py)^{n+}$ being present, and a peak at 286.6 eV due to the C-O groups (from G-O) and C-N groups (from $C_{60}(Py)^{n+}$). The N1s spectra (inset) of the $C_{60}(Py)^{n+}$ salt and the $[C_{60}(Py)^{n+}]G-O$ film show two peaks at 402.0 and 399.3 eV corresponding to **Py** (cationic N) and pyrrolidine (non-ionic N) groups²³. The ratio of **Py** to pyrrolidine groups is estimated to be 4.8 for the $C_{60}(Py)^{n+}$ salt (83% **Py**) and 1.2 for the $[C_{60}(Py)^{n+}]G-O$ film (52% **Py**). Note that **Py** with protonated tertiary amine can be converted to pyrrolidine through deprotonation²³.

¹H and 2-Dimensional (2D) solution-state NMR spectra were acquired on the $C_{60}(Py)^{n+}$ salt to probe its structure (**Figs. S12-16**). There are mainly two groups of peaks in the ¹H NMR spectrum (**Fig. S12**) corresponding to the CH₂ (4.4 to 5.6 ppm) and CH₃ (3.3 to 4.1 ppm) protons from the **Py** groups in $C_{60}(Py)^{n+}$. These peaks are broad and complex, indicating the presence of many different $C_{60}(Py)^{n+}$ isomers. The CH₂ and CH₃ peaks have an integral ratio of 0.68 (very close to 2:3), consistent with the presence of **Py** groups. The ¹H and ¹³C chemical shifts of the CH₃ peaks are also consistent with the CH₃ being attached to a positively charged, quaternary N. Furthermore, the CH₂ and CH₃ protons show both multiple-bond correlations (¹H-¹³C HMBC, **Fig. S14**) and single-bond correlations (HSQC, **Fig. S15**) to their respective

carbon atoms, indicating symmetry in the **Py** group and hence the presence of the cationic dimethyl ammonium moiety. High-resolution nanoelectrospray ionisation mass spectrometry (nESI-MS)²⁴ was used to determine the extent of the cationic functionalisation in the $C_{60}(\text{Py})^{n+}$ salt (**Fig. S17**; **Tables S1** and **S2**) and the weighted average number of **Py** groups per C_{60} molecule in the $C_{60}(\text{Py})^{n+}$ salt was measured to be about 2.7.

¹H solid-state NMR (SS-NMR) gives information regarding the native state of G-O, the $C_{60}(\text{Py})^{n+}$ salt, and the $[C_{60}(\text{Py})^{n+}]$ G-O film (**Fig. 3c**). The ¹H spectrum of the pure G-O is broad, with the main peak centred at 5 ppm corresponding to the COH moieties, and a broad shoulder at 7 ppm for the aromatic proton species (HC_{ar}). In comparison, the $C_{60}(\text{Py})^{n+}$ salt produces a sharp signal at 3.5 ppm for the NCH_3 moiety and a broad shoulder at 4.5 ppm for the NCH_2 moiety. The $[C_{60}(\text{Py})^{n+}]$ G-O film gives a ¹H NMR signal that shows the presence of moieties from both G-O and $C_{60}(\text{Py})^{n+}$, given that the shoulder for the aromatic signals from G-O is clearly assignable, as well as the signal of the NCH_3 moieties from **Py** groups. Note that the broadening of the NCH_3 signal in the $[C_{60}(\text{Py})^{n+}]$ G-O film indicates a significant reduction in molecular motion likely due to steric or electrostatic interactions with the negatively charged G-O. Thus, the ¹H SS-NMR spectrum provides strong evidence of the intercalation of $C_{60}(\text{Py})^{n+}$ in the G-O film.

To evaluate whether the $C_{60}(\text{Py})^{n+}$ is inserted between the G-O layers and also whether it forms separate phases, ¹H 2D exchange SS-NMR spectra were acquired (**Fig. 3e**). Here ¹H spin diffusion results in an exchange of signals between different ¹H moieties in nanometre scale proximity. Taking a 1D parallel slice at the position of the aromatic ¹H species, we observed the change in the intensity of the NCH_3 species as a function of spin diffusion time during which the signal is transferred from HC_{ar} to

NCH₃ as seen in the 1D spectra in **Fig. 3d** (note that the spin exchange process is symmetric, and taking a 1D slice at the NCH₃ position yields signal transfer from NCH₃ to HC_{ar}). The observed sub-millisecond spin exchange between the HC_{ar} from G-O and the NCH₃ from C₆₀(Py)ⁿ⁺ provides evidence of the sub-nanometre proximity of C₆₀(Py)ⁿ⁺ and the G-O film.

Water permeation through G-O and [C₆₀(Py)ⁿ⁺]G-O membranes. G-O membranes have a high water permeability due to their porous structure,²⁵ and adjusting the interlayer distance through insertion of ions or molecules has been reported to change the water transport through these membranes^{15,26}. We have examined vapour and liquid water permeation rates through the G-O and [C₆₀(Py)ⁿ⁺]G-O membranes prepared from 2 mL of G-O dispersion, as shown in **Fig. 4**. A water vapour flux of 0.800 (±0.065) L m⁻² h⁻¹ for the [C₆₀(Py)ⁿ⁺]G-O membrane was obtained, which is 6.8 times that of the flux for the G-O membrane, 0.117 (±0.005) L m⁻² h⁻¹. Furthermore, the flux for the [C₆₀(Py)ⁿ⁺]G-O membrane was marginally smaller than that for the porous support filter (0.2 μm pore size), 0.847 (±0.030) L m⁻² h⁻¹, suggesting that water vapour experienced little resistance when moving through the [C₆₀(Py)ⁿ⁺]G-O membrane. The liquid water flux rate for the [C₆₀(Py)ⁿ⁺]G-O membrane in dead-end filtration was 34.5 (±2.6) L m⁻² h⁻¹, which is 10.5 times higher than that of the G-O membrane, 3.28 (±0.16) L m⁻² h⁻¹. The support filter had a significantly higher water flux of 16,700 (±900) L m⁻² h⁻¹, showing little effect on the liquid water permeation of the membranes (**Fig. S18**). The increased interlayer spacing of the [C₆₀(Py)ⁿ⁺]G-O membrane could be the reason for its superior water flux.

Graphitisation of the [C₆₀(Py)ⁿ⁺]G-O film. Thermal decomposition of G-O, the C₆₀(Py)ⁿ⁺ salt, and the [C₆₀(Py)ⁿ⁺]G-O film was examined by thermogravimetric

analysis coupled with mass spectrometry (TGA-MS) (**Fig. S20**). The major weight loss of G-O occurred between 150-250 °C (26.8 wt.%) with a release of H₂O and CO₂. The C₆₀(Py)ⁿ⁺ salt decomposed above 200 °C (34.8 wt.%, 200-350 °C), evolving various gases (H₂O, NO/NO₂, CO₂ and SO₂) and multi-stage decomposition was observed for the [C₆₀(Py)ⁿ⁺]G-O film, with NO/NO₂ species being released around 100 °C followed by a major release of gases (H₂O, NO/NO₂ and CO₂) between 150-250 °C. These results indicate the presence of C₆₀(Py)ⁿ⁺ (contributing N-containing species) and the absence of sulfate ions (contributing S-containing species) in the [C₆₀(Py)ⁿ⁺]G-O film, consistent with our other analyses.

Thermal decomposition caused dramatic changes in structure and composition of the films, as shown by XRD (**Fig. S21**), XPS (**Fig. S22**) and Raman spectra (**Fig. S23**). Notably, an XRD peak corresponding to a d-spacing of 0.34 nm was observed for the reduced G-O film, whereas the decomposed [C₆₀(Py)ⁿ⁺]G-O film showed two peaks of 0.34 and 0.41 nm, suggesting the possible presence of residues from the decomposition of C₆₀(Py)ⁿ⁺ between the layers. N remained in the decomposed C₆₀(Py)ⁿ⁺ salt (1.35 at%) and decomposed [C₆₀(Py)ⁿ⁺]G-O film (1.30 at.%) while S was completely absent. A significant change in the Raman spectrum was seen for the C₆₀(Py)ⁿ⁺ salt after decomposition, with the appearance of D and G bands indicating a disordered carbon structure. TEM images (**Fig. S24**) show a fullerene-like amorphous structure with highly curved planes, possibly composed of C₆₀ fragments formed during decomposition. Heating at 2000 °C (under applied pressure in vacuum) or at 2700 °C (without physical confinement in vacuum) converted the [C₆₀(Py)ⁿ⁺]G-O films into highly graphitised structures, as shown by Raman spectra (**Fig. S23**), XRD (**Fig. S25**) and cross-sectional TEM (**Fig. S26**).

In conclusion, we have prepared a “stage-1” intercalated structure by the ion exchange of “cationic C₆₀” into G-O films, which resulted in a fairly uniform expansion of the interlayer distance. The strong affinity between “cationic C₆₀” and G-O enabled the intercalated film to remain stable in various liquid media (including water), and its water permeability as a membrane was studied. Rapid transport of water vapour with almost no resistance was observed for the intercalated G-O membranes, and a significantly increased liquid water flux was found compared to G-O membranes. These membranes might therefore be useful for molecular or ionic sieving.

Experimental Section

Preparation of G-O and [C₆₀(Py)ⁿ⁺]G-O films. A water-soluble, “cationic C₆₀” (C₆₀-n-(*N,N*-dimethylpyrrolidinium sulfate); Solaris Chem Inc. (Product # SOL5262) was used without further modification. G-O platelets were prepared by the exfoliation of graphite oxide synthesised using the modified Hummers method, and the detailed preparation procedure has been described in previous reports^{27,28}. The lateral size of the G-O platelets ranged from 1-30 μm (**Fig. S1**). G-O films were prepared by filtering a specific volume (2, 5, or 15 mL) of the G-O dispersion (0.5 mg/mL) through mixed cellulose ester (MCE) filters (WhatmanTM, 10401712, 0.2 μm pore size, 47-mm diameter), before drying in air. The thinner G-O films (from 2 or 5 mL volumes) were left on the filters while those prepared from 15 mL dispersion were separated from the filters. The resulting G-O films were rinsed in Milli-Q water before immersing them in a C₆₀(Py)ⁿ⁺ salt solution (0.5 mg/mL). After soaking, the films were collected, washed with water, and dried in air. The mass change of the films was measured at 21 °C under a relative humidity of 38%.

Material Characterisation. XRD patterns were obtained using an Empyrean Thin-Film XRD unit and analysed using X’Pert HighScore Plus software. SEM images were recorded on a FEI Nova NanoSEM 450 FE-SEM. AFM images were acquired on a Bruker Dimension ICON SPM operating in the tapping mode. A G-O dispersion was drop-cast onto a freshly cleaved mica substrate and dried in air. The [C₆₀(Py)ⁿ⁺]G-O was prepared by adding a drop of the salt solution onto the G-O-loaded substrate. After resting for 5 min, the surface was repeatedly washed with water, and dried in air prior to AFM imaging. AFM images were analysed using the Gwyddion SPM software. Contact angle measurements were obtained using a Rame-Hart goniometer. TEM specimens (**Figs. 2a and 2b**) were prepared by drop casting a

G-O dispersion onto a holey carbon-coated Cu grid (SPI Supplies, #2450-AB) and dried in air. The grid was then immersed in the salt solution for 30 min, prior to gentle washing with water and drying in air. FIB specimens were fabricated using an FEI Nova Nanolab 200 unit. TEM analysis was performed using a JEOL JEM-F200 Multi-Purpose FEG-S/TEM operating at an accelerating voltage of 80 kV. Image J and Pathfinder were used for processing the TEM and elemental map images. FTIR was recorded on a Spectrum 100/Spotlight 400 spectrometer in the ATR mode. XPS spectra were acquired using an ESCALAB 250 Xi, Thermo Scientific. Combustion elemental analysis was conducted on an Elementar varioMACRo cube for C, H, N, and S and a rapidOXY cube for O. The ^1H and 2D solution-state NMR spectra were acquired on a Bruker AVANCE III HD 600 spectrometer equipped with a 5 mm TCI cryoprobe, operating at frequencies of 600 MHz and 151 MHz for the ^1H and ^{13}C nuclei, respectively. The ^1H spectra were calibrated by assigning the HDO residual solvent peak to 4.70 ppm. nESI-MS was performed using an LTQ Orbitrap XL (Thermo Scientific, Waltham, MA). Full details are provided in the Supporting Information. ^1H solid-state NMR was acquired on a Bruker AVANCE III 700 MHz spectrometer with a 16.4 tesla superconducting magnet, operating at a frequency of 700 MHz for the ^1H nucleus. Approximately 10 mg of sample was packed in a glove box in 2.5 mm zirconia rotors fitted with Vespel® caps and spun to 30 kHz at the magic angle in a triple resonance 2.5 mm HXY MAS probehead. A ^1H 90° pulse length of 2.5 μs was used with sufficient recycle delay to ensure full signal relaxation. The ^1H 2D exchange data sets were acquired with ^1H spin diffusion times of 0.1 to 3 ms. The 2D data set was acquired with 128 rotor synchronised increments of 33.33 μs in the indirect dimension. The ^1H chemical shifts were referenced to adamantane at 1.8 ppm. TGA-MS analysis was performed using a combined TGA Q500 Auto (TA

Instruments) and MS QGA (Hiden Analytical LLC) by heating to 500 °C with a heating rate of 10 °C/min under Ar. Raman spectra were recorded on a Renishaw InVia 2 Raman spectrometer at room temperature with a 532 nm laser excitation.

Membrane permeation experiments. G-O membranes were prepared by vacuum-filtering 2 mL of the G-O dispersion through MCE filters, following the procedure described above. The membranes were immersed in the (C_{60} -n-(*N,N*-dimethylpyrrolidinium sulfate)) salt solution for 3 days before being gently washed with water and drying in air. For the water vapour permeation tests, the membrane was sandwiched between waterproof tape giving an effective area of 1.13 cm² (**Fig. S19c**). The tests were carried out using the homemade setup illustrated in **Fig. S19a**. The prepared membrane was sandwiched between a glass funnel (feed side) and a sintered glass filter (permeate side), where a 28-mbar vacuum pressure was applied using a diaphragm pump (V-700, Büchi). An in-line cold finger was used to condense the permeate in an ice bath. On the feed side, water (10 mL) at a temperature maintained at 22-24 °C was added. There is an air gap between the membrane and water. To evaluate the performance of the membranes, the mass of the water that remained on the feed side before and after 28 h was measured and subtracted to determine the volume of water (V , mL) that had permeated the membrane. For each membrane, the vapour permeation experiment was carried out 3 times using a new membrane each time. The water flux (J) was calculated using the following formula:

$$J = V/(A_{eff}t) \quad (1)$$

Where J is the water flux (mL m⁻² h⁻¹), V is the permeate volume (L), A_{eff} is the membrane effective area, and t is the time (h).

The dead-end filtration was carried out using a stirred cell (Amicon®) shown in **Fig. S19b**. The membranes were sandwiched between waterproof tape for an effective area

of 4.91 cm² (**Fig. S19c**). Water (20 mL) was added into the cell and pressurised nitrogen gas was used to apply a pressure of 1 bar. To measure the water flux for each membrane, Equation 1 was used. The time taken for the volume of water to pass through the membrane, t , was determined with a mass balance that recorded the mass of the permeate at 1 s intervals (**Fig. S18**). For each membrane, dead-end filtration was carried out 3 times using a new membrane each time.

Graphitisation of the [C₆₀(Py)ⁿ⁺]G-O film. Heating was carried out in a hot press furnace at 2000 °C under vacuum or in a graphite furnace at 2700 °C under vacuum with a heating rate of 10 °C/min, 1 h holding time and cooling to ambient conditions in the furnace. For the 2000 °C treatment, the sample film (17-mm in diameter, roughly 5-µm thick) was sandwiched between stacked graphite spacers (22-mm in diameter, 3-mm thick), and a pressure of 20 MPa was applied to the film and maintained for the entire heating and cooling process.

Acknowledgements

This study was supported by the Australian Research Council (DE180100294) and the Institute for Basic Science (IBS-R019-D1). The authors appreciate Chuan Zhao for sharing laboratory space; Charlie Kong and Qiang Zhu for FIB specimen preparation; Zhaoquan Zhang and Wugang Fan for assistance in graphitisation experiments; Anne Poljak and Yu Wang for discussions on experimental results. The authors thank the Mark Wainwright Analytical Centre at the University of New South Wales for access to the analytical instruments.

Author Contributions

X.C. and R.S.R conceived the study and designed and analysed the experiments; X.C. performed the synthesis and characterisations of materials; K.C. contributed to the membrane permeation experiments; A.R. performed the ^1H solid-state NMR analysis; D.J.L. carried out the ^1H and 2D solution-state NMR analysis; M.T. and W.A.D. performed the nESI-MS experiments and analysed the result; S.H.L. carried out the TGA-MS measurements. X.C. and R.S.R primarily wrote the various manuscript versions, and all authors contributed to writing and reviewing the manuscripts.

Additional information

Supplementary Information

Competing financial interests: The authors declare no competing financial interests.

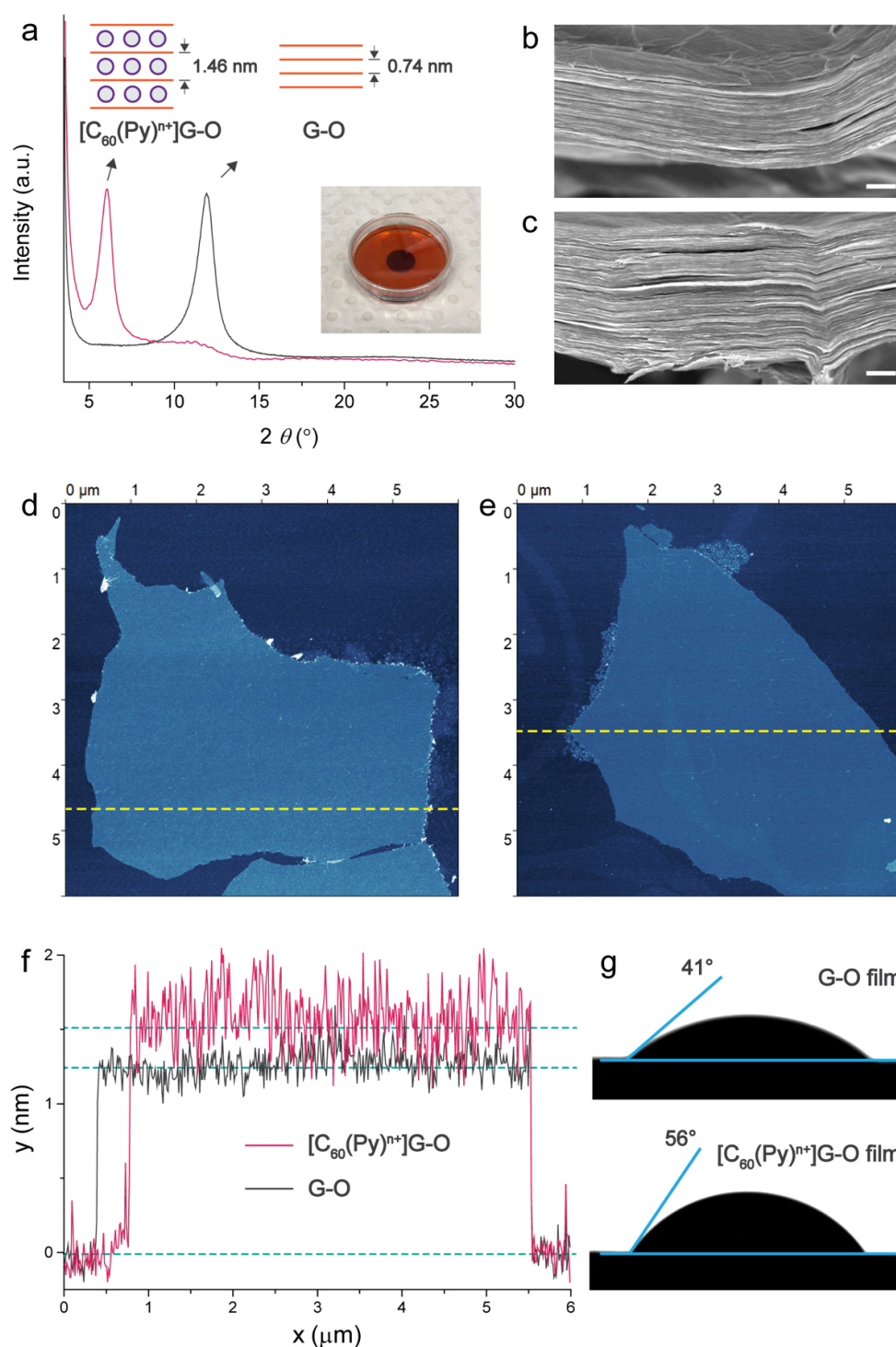


Figure 1. “Stage-1” intercalation of “cationic C_{60} ” into G-O films. (a) XRD patterns of G-O and $[C_{60}(Py)^{n+}]G-O$ films, with schematics illustrating the intercalation of $C_{60}(Py)^{n+}$ into G-O layers. Inset: photograph of a G-O film soaking in the $C_{60}(Py)^{n+}$ salt solution. (b, c) SEM images of fracture cross-sectional surfaces of the G-O films before (b) and after (c) $C_{60}(Py)^{n+}$ intercalation. Scale bars, 1 μm . (d, e) AFM images of a single layer of G-O platelet (d), and a G-O with $C_{60}(Py)^{n+}$ adsorbed on the surface (e). (f) AFM height scans along the dashed lines in (d) and (e). (g) Contact angle measurements of G-O and $[C_{60}(Py)^{n+}]G-O$ films.

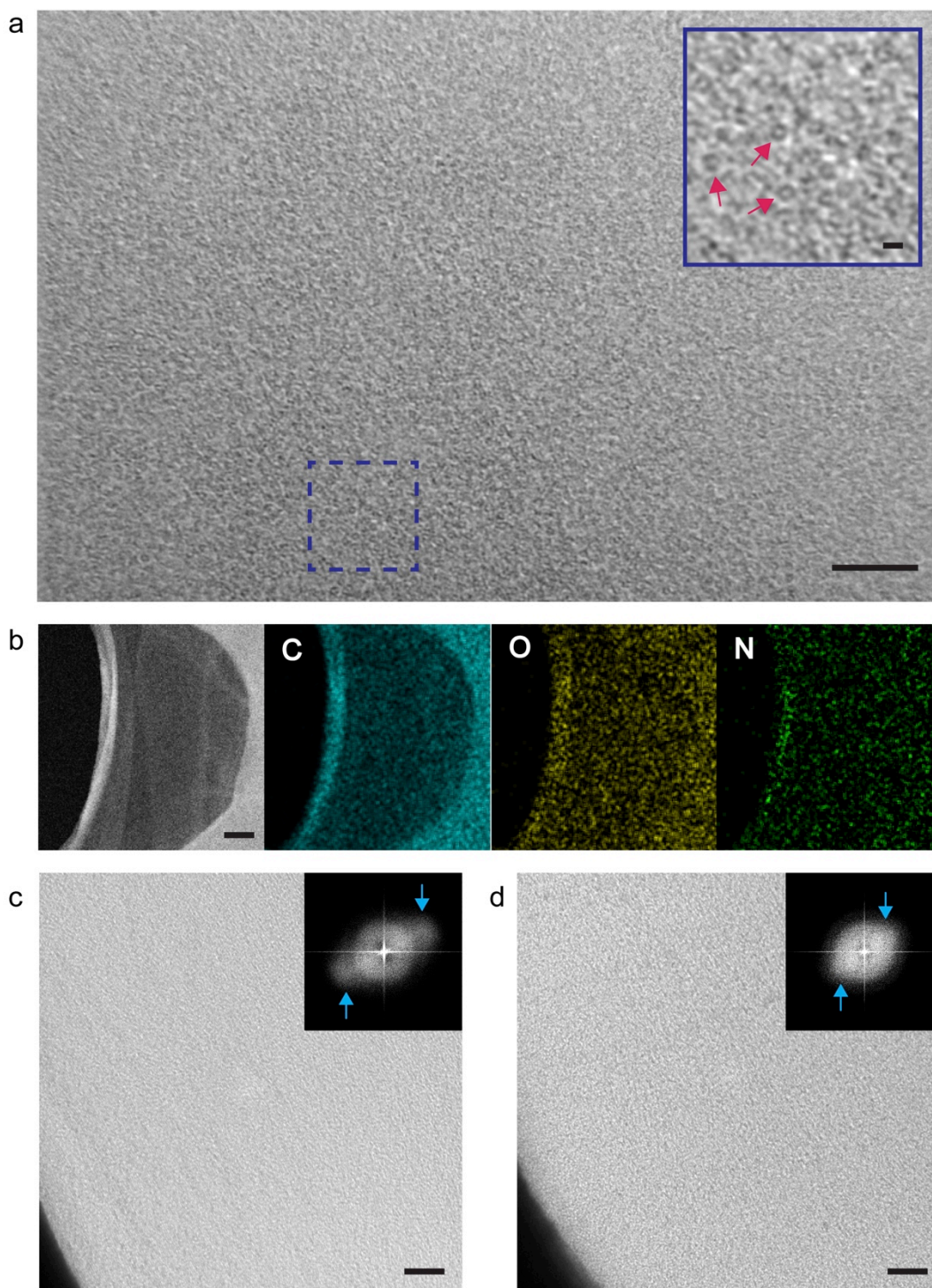


Figure 2. TEM images of the G-O and [C₆₀(Py)ⁿ⁺]G-O films. (a) HRTEM image from [C₆₀(Py)ⁿ⁺]G-O, with the inset showing a magnified region. The arrows indicate the C₆₀(Py)ⁿ⁺ attached on the surface of G-O. Scale bars, 10 nm; (inset, 1 nm). (b) Elemental (C, O, and N) maps of the [C₆₀(Py)ⁿ⁺]G-O film. Scale bar, 100 nm. Cross-sectional (c, d) TEM images of FIB-fabricated G-O film (c) and [C₆₀(Py)ⁿ⁺]G-O film (d), with the insets showing FFT patterns converted from the corresponding TEM images. Scale bars, 10 nm.

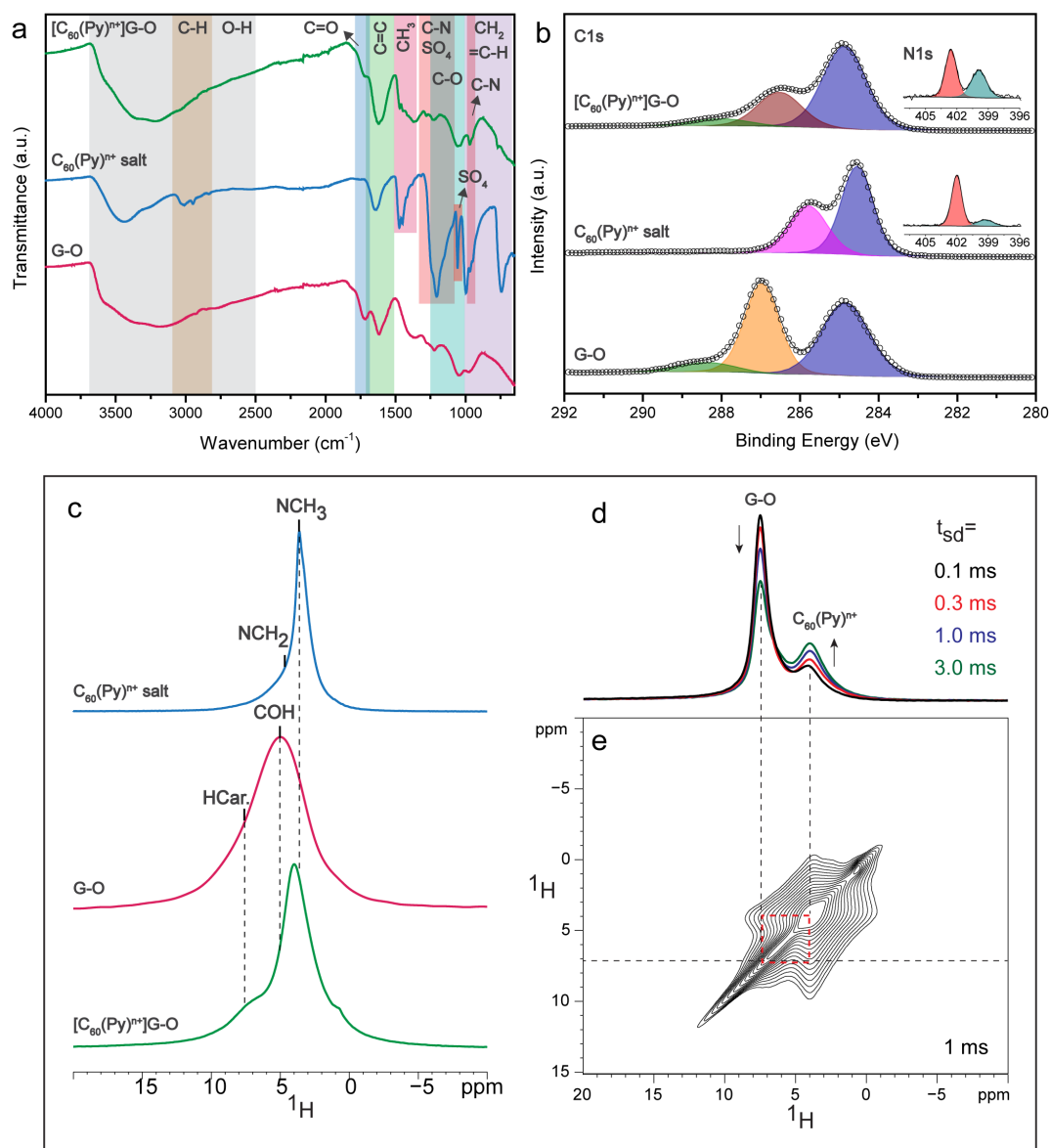


Figure 3. Spectroscopic analysis of G-O, the $C_{60}(\text{Py})^{n+}$ salt and the $[C_{60}(\text{Py})^{n+}]G-O$ film. (a) FTIR spectra, (b) XPS C1s and N1s spectra, (c) solid-state ^1H NMR of G-O, the $C_{60}(\text{Py})^{n+}$ salt and the $[C_{60}(\text{Py})^{n+}]G-O$ film. (d) 1D extracts from a series of ^1H - ^1H 2D exchange spectra with varying ^1H spin diffusion times (t_{sd}). (e) Example ^1H - ^1H 2D exchange experiment with 1 ms of spin diffusion. The horizontal dashed line shows the position of the extracted 1D slices, plotted above the 2D spectrum. Vertical dashed lines are guides for the eye, while the red dashed square shows the position of the on-diagonal and off-diagonal peaks.

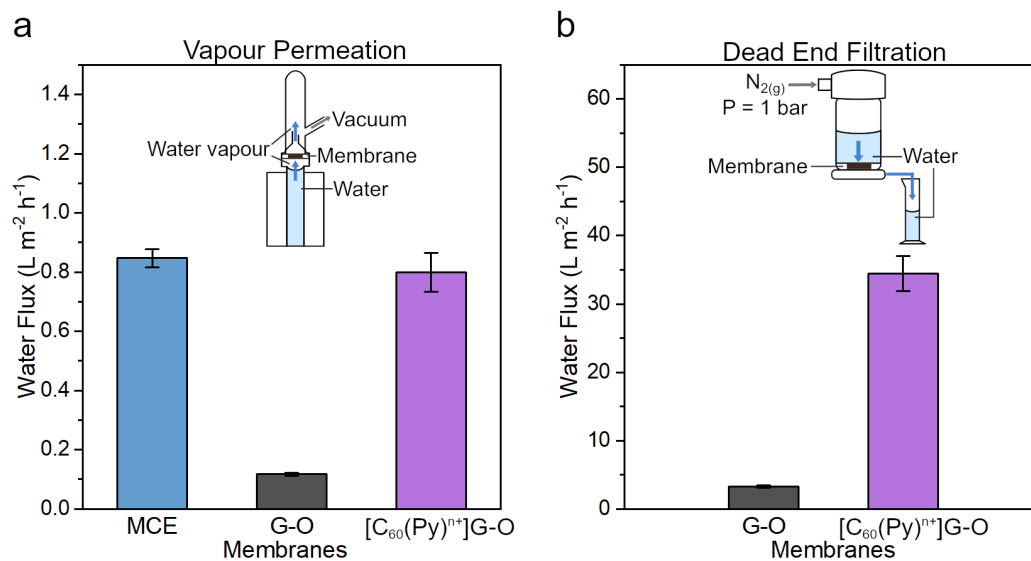


Figure 4. Water permeation through the G-O and $[C_{60}(Py)^{n+}]G-O$ membranes. (a) Water flux for vapour permeation and (b) dead-end filtration for MCE, G-O and $[C_{60}(Py)^{n+}]G-O$ membranes, with insets illustrating the experimental setup. The water flux for the MCE filter in dead-end filtration (b) is $16,700 (\pm 900) L m^{-2} h^{-1}$.

Reference

1. Smith, B. W.; Monthieux, M.; Luzzi, D. E. Encapsulated C₆₀ in Carbon Nanotubes. *Nature* **1998**, *396*, 323-324.
2. Mirzayez, R.; Mustonen, K.; Monazam, M. R. A.; Mittelberger, A.; Pennycook, T. J.; Mangler, C.; Susi, T.; Kotakoski, J.; Meyer, J. C. Buckyball Sandwiches. *Sci. Adv.* **2017**, *3* (6), e1700176.
3. Saito, S.; Oshiyama, A. Design of C₆₀-Graphite Cointercalation Compounds. *Phys. Rev. B* **1994**, *49*, 17413-17419.
4. Fuhrer, M. S.; Hou, J. G.; Xiang, X. D.; Zettl, A. C₆₀ Intercalated Graphite: Predictions and Experiments. *Solid State Commun.* **1994**, *90* (6), 357-360.
5. Spyrou, K.; Kang, L.; Diamanti, E. K.; Gengler, R. Y.; Gournis, D.; Prato, M.; Rudolf, P. A Novel Route towards High Quality Hüllerene-Pillared Graphene. *Carbon* **2013**, *61*, 313-320.
6. Hummers, W. S.; Offeman, R. E. Preparation of Graphitic Oxide. *J. Am. Chem. Soc.* **1958**, *80* (6), 1339-1339.
7. Dikin, D. A.; Stankovich, S.; Zimney, E. J.; Piner, R. D.; Dommett, G. H. B.; Evmenenko, G.; Nguyen, S. T.; Ruoff, R. S. Preparation and Characterization of Graphene Oxide Paper. *Nature* **2007**, *448*, 457-460.
8. Dimiev, A. M.; Alemany, L. B.; Tour, J. M. Graphene Oxide. Origin of Acidity, Its Instability in Water, and a New Dynamic Structural Model. *ACS Nano* **2013**, *7* (1), 576-588.
9. Stankovich, S.; Dikin, D. A.; Compton, O. C.; Dommett, G. H. B.; Ruoff, R. S.; Nguyen, S. T. Systematic Post-assembly Modification of Graphene Oxide Paper with Primary Alkylamines. *Chem. Mater.* **2010**, *22* (14), 4153-4157.

10. Bourlinos, A. B.; Gournis, D.; Petridis, D.; Szabó, T.; Szeri, A; Dékány, I.
Graphite Oxide: Chemical Reduction to Graphite and Surface Modification with
Primary Aliphatic Amines and Amino Acids. *Langmuir* **2003**, *19* (15), 6050-6055.
11. Matsuo, Y.; Miyabe, T.; Fukutsuka, T.; Sugie, Y. Preparation and
Characterization of Alkylamine-Intercalated Graphite Oxides. *Carbon* **2007**, *45*
(5), 1005-1012.
12. Tsoufis, T.; Tuci, G.; Caporali, S.; Gournis, D.; Giambastiani, G. *p*-
Xylylenediamine Intercalation of Graphene Oxide for the Production of Stitched
Nanostructures with a Tailored Interlayer Spacing. *Carbon* **2013**, *59*, 100-108.
13. Spyrou, K.; Potsi, G.; Diamanti, E. K.; Ke, X.; Serestatidou, E.; Verginadis, I. I.;
Velalopoulou, A. P.; Evangelou, A. M.; Deligiannakis, Y.; Van Tendeloo, G.;
Gournis, D.; Rudolf, P. Towards Novel Multifunctional Pillared Nanostructures:
Effective Intercalation of Adamantylamine in Graphene Oxide and Smectite
Clays. *Adv. Funct. Mater.* **2014**, *24* (37), 5841-5850.
14. Spyrou, K.; Calvaresi, M.; Diamanti, E. K.; Tsoufis, T.; Gournis, D.; Rudolf, P;
Zerbetto, F. Graphite Oxide and Aromatic Amines: Size Matters. *Adv. Funct.*
Mater. **2015**, *25* (2), 263-269.
15. Chen, L.; Shi, G.; Shen, J.; Peng, B.; Zhang, B.; Wang, Y.; Bian, F.; Wang, J.; Li,
D.; Qian, Z.; Xu, G.; Liu, G.; Zeng, J.; Zhang, L.; Yang, Y.; Zhou, G.; Wu, M.;
Jin, W.; Li, J.; Fang, H. Ion Sieving in Graphene Oxide Membranes via Cationic
Control of Interlayer Spacing. *Nature* **2017**, *550*, 380-383.
16. Park, S.; Ruoff, R. S. Chemical Methods for the Production of Graphenes. *Nature*
Nanotechnol. **2008**, *4*, 217-224.
17. Huang, K.; Rowe, P.; Chi, C.; Sreepal, V.; Bohn, T.; Zhou, K. G.; Su, Y.; Prestat,
E.; Balakrishna Pillai, P.; Cherian, C. T.; Michaelides, A.; Nair, N. N. Cation-

- Controlled Wetting Properties of Vermiculite Membranes and Its Promise for Fouling Resistant Oil–Water Separation. *Nature Commun.* **2020**, *11*, 1097.
18. Quéré, D. Rough Ideas on Wetting. *Physica A* **2002**, *313* (1-2), 32-46.
19. Moon, I. K.; Lee, J.; Ruoff, R. S.; Lee, H. Reduced Graphene Oxide by Chemical Graphitization. *Nature Commun.* **2010**, *1*, 73.
20. Acik, M.; Lee, G.; Mattevi, C.; Chhowalla, M.; Cho, K.; Chabal, Y. J. Unusual Infrared-Absorption Mechanism in Thermally Reduced Graphene Oxide. *Nature Mater.* **2010**, *9*, 840-845.
21. Dimiev, A.; Kosynkin, D. V.; Alemany, L. B.; Chaguine, P.; Tour, J. M. Pristine Graphite Oxide. *J. Am. Chem. Soc.* **2010**, *134* (5), 2815-2822.
22. Kim, S.; Zhou, S.; Hu, Y.; Acik, M.; Chabal, Y. J.; Berger, C.; de Heer, W. A.; Bongiorno, A.; Reid, E. Room-Temperature Metastability of Multilayer Graphene Oxide Films. *Nature Mater.* **2012**, *11*, 544-549.
23. Senthilkumar, K.; Prabakar, S. J. R.; Park, C.; Jeong, S.; Lah, M. S.; Pyo, M. Graphene Oxide Self-Assembled with a Cationic Fullerene for High Performance Pseudo-Capacitors. *J. Mater. Chem. A* **2016**, *4*, 1663-1670.
24. Nguyen, G. T. H.; Tran, T. N.; Podgorski, M. N.; Bell, S. G.; Supuran, C. T.; Donald, W. A. Nanoscale Ion Emitters in Native Mass Spectrometry for Measuring Ligand–Protein Binding Affinities. *ACS Cent. Sci.* **2019**, *5* (2), 308–318.
25. Boehm, H. P.; Clauss, A.; Hofmann, U. Graphite Oxide and Its Membrane Properties. *J. Chim. Phys.* **1961**, *58*, 141-147.
26. Tang, X.; Qu, Y.; Deng, S. L.; Tan, Y. Z.; Zhang, Q.; Liu, Q. Fullerene-Regulated Graphene Oxide Nanosheet Membranes with Well-Defined Lamellar

Nanochannels for Precise Molecule Sieving. *J. Mater. Chem. A* **2018**, *6*, 22590-22598.

27. Chen, X.; Meng, D.; Wang, B.; Li, B.-W.; Li, W.; Bielawski, C. W.; Ruoff, R. S. Rapid Thermal Decomposition of Confined Graphene Oxide Films in Air. *Carbon* **2016**, *101*, 71-76.

28. Chen, X.; Li, W.; Luo, D.; Huang, M.; Wu, X.; Huang, Y.; Lee, S. H.; Chen, X.; Ruoff, R. S. Controlling the Thickness of Thermally Expanded Films of Graphene Oxide. *ACS Nano* **2017**, *11* (1), 665-674.

Supplementary Information

Stage-1 cationic C₆₀ intercalated graphene oxide films

Xianjue Chen,^{1,*} Karin Ching,¹ Aditya Rawal,² Douglas J. Lawes,² Mohammad Tajik,¹ William A. Donald,¹ Sun Hwa Lee,³ and Rodney S. Ruoff^{3,4,5,6,*}

¹ *School of Chemistry, University of New South Wales, Sydney, New South Wales 2052, Australia*

² *Mark Wainwright Analytical Centre, University of New South Wales, Sydney, New South Wales 2052, Australia*

³ *Center for Multidimensional Carbon Materials (CMCM), Institute for Basic Science (IBS), Ulsan 44919, Republic of Korea*

⁴ *Department of Chemistry, Ulsan National Institute of Science and Technology (UNIST), Ulsan 44919, Republic of Korea*

⁵ *School of Materials Science and Engineering, Ulsan National Institute of Science and Technology (UNIST), Ulsan 44919, Republic of Korea*

⁶ *School of Energy and Chemical Engineering, Ulsan National Institute for Science and Technology (UNIST), Ulsan 44919, Republic of Korea*

**Email: correspondence and requests for materials should be addressed to X.C.*

(xianjue.chen@unsw.edu.au) and R.S.R. (ruofflab@gmail.com)

Table of Contents	2
Fig. S1. SEM images of as-prepared G-O platelets	3
Fig. S2. <i>Ex situ</i> thin-film XRD patterns of “2-mL” and “5-mL” G-O films	4
Fig. S3. Powder XRD pattern of the C ₆₀ (Py) ⁿ⁺ salt	5
Fig. S4. C ₆₀ (Py) ⁿ⁺ intercalation into G-O films	6
Fig. S5. Stability of [C ₆₀ (Py) ⁿ⁺]G-O films against soaking in organic solvents	7
Fig. S6. Stability of [C ₆₀ (Py) ⁿ⁺]G-O films against ion exchange	8
Fig. S7. Stability of [C ₆₀ (Py) ⁿ⁺]G-O films against “shock cooling”	9
Fig. S8. Stability of [C ₆₀ (Py) ⁿ⁺]G-O films against heating	10
Fig. S9. Stability of [C ₆₀ (Py) ⁿ⁺]G-O films against HI treatment	11
Fig. S10. TEM analysis of the C ₆₀ (Py) ⁿ⁺ salt on CVD-grown graphene	12
Fig. S11. XPS full surveys of G-O film, C ₆₀ (Py) ⁿ⁺ salt, and [C ₆₀ (Py) ⁿ⁺]G-O film	13
Fig. S12. ¹ H solution-state NMR spectrum of the C ₆₀ (Py) ⁿ⁺ salt	14
Fig. S13. ¹ H solution-state NMR spectrum showing the ratio of CH ₂ and CH ₃	15
Fig. S14. ¹ H- ¹³ C HMBC NMR spectrum of the C ₆₀ (Py) ⁿ⁺ salt	16
Fig. S15. ¹ H- ¹³ C HSQC NMR spectrum of the C ₆₀ (Py) ⁿ⁺ salt	17
Fig. S16. ¹ H inversion-recovery NMR spectrum of the C ₆₀ (Py) ⁿ⁺ salt	18
Fig. S17. nESI-MS spectra for of the C ₆₀ (Py) ⁿ⁺ salt	19
Table S1. Summary of nESI-MS results for the C ₆₀ (Py) ⁿ⁺ salt	20
Table S2. Relative amounts of each Py-functionalised C ₆₀ derivatives	21
Fig. S18. Record of permeated water mass for dead-end filtration	22
Fig. S19. Schematic of vapour permeation and dead-end filtration	23
Fig. S20. TGA-MS of G-O, the C ₆₀ (Py) ⁿ⁺ salt, and the [C ₆₀ (Py) ⁿ⁺]G-O film	24
Fig. S21. XRD of samples after thermal treatment	25
Fig. S22. XPS of samples after thermal treatment	26
Fig. S23. Raman spectra of samples before and after thermal treatment	27
Fig. S24. TEM of residues from thermal decomposition of the C ₆₀ (Py) ⁿ⁺ salt	28
Fig. S25. XRD of the graphitised [C ₆₀ (Py) ⁿ⁺]G-O films	29
Fig. S26. Cross-sectional TEM image of the graphitised [C ₆₀ (Py) ⁿ⁺]G-O film	30
References	31

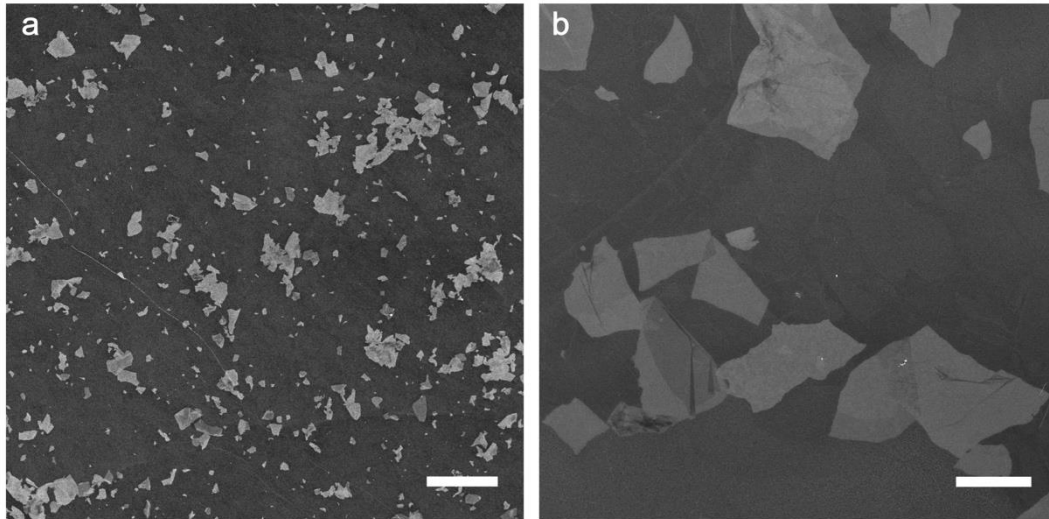


Figure S1. SEM images of as-prepared G-O platelets on HOPG. Scale bars, **(a)** 50 μm ; **(b)** 5 μm .

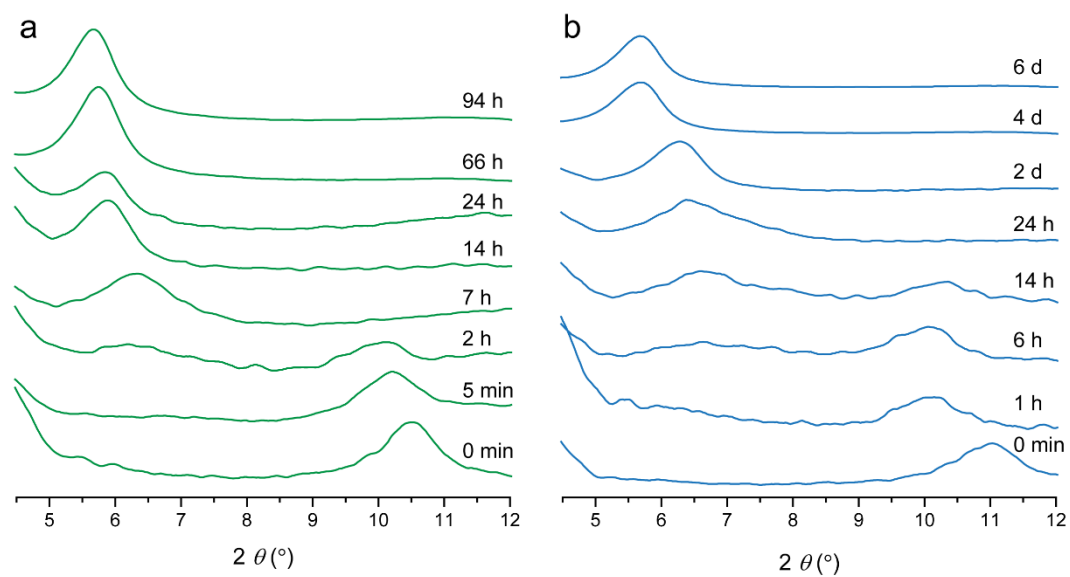


Figure S2. *Ex situ* thin-film XRD patterns of (a) "2-mL" and (b) "5-mL" G-O films after soaking in $C_{60}(Py)^{n+}$ salt solution for different durations.

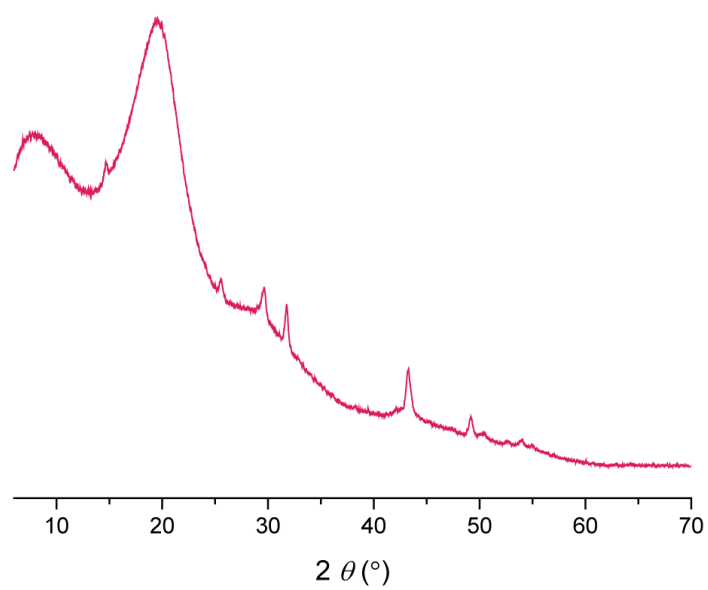


Figure S3. Powder XRD pattern of the $C_{60}(Py)^{n+}$ salt.

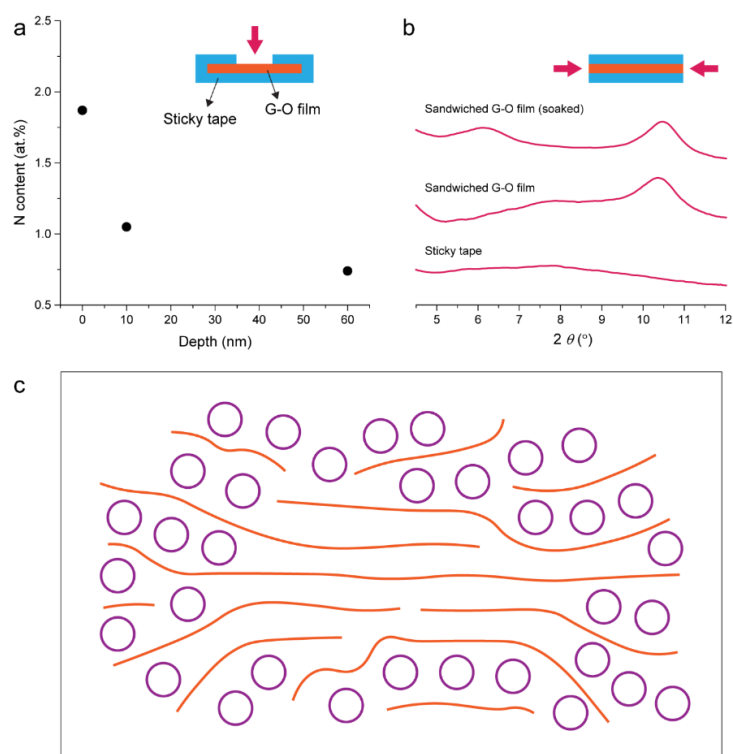


Figure S4. (a) N content on the surface and in the subsurface of the G-O film after 30-min soaking in the $C_{60}(Py)^{n+}$ salt solution. (b) XRD patterns of the sticky tape and “sandwiched” G-O film before and after 3-day soaking in the $C_{60}(Py)^{n+}$ salt solution. Insets are schematics showing different configurations of the prepared G-O films. (c) An illustration of the $C_{60}(Py)^{n+}$ intercalation into a G-O film from a cross-sectional view, circles: $C_{60}(Py)^{n+}$; lines: G-O platelets.

To reveal the intercalation paths for $C_{60}(Py)^{n+}$, the G-O films were prepared in two configurations with waterproof sticky tape. In the first, the edge and one side of the G-O film were sealed using the tape with a “window” open on the other side so that only this surface was exposed to the $C_{60}(Py)^{n+}$ salt solution. After 30-min soaking, the film was collected, washed with water, and dried in air. XPS depth profiling detected N (the “tracer” element for $C_{60}(Py)^{n+}$) on the surface and 60 nm under the surface, and the concentration decreased with depth (**Fig. S4a**). This suggests that $C_{60}(Py)^{n+}$ can enter the film from the surface. In the other case, the film was “sandwiched” using the tape with only the film edges in contact with the salt solution. The film was collected after soaking for 3 days. XRD (**Fig. S4b**) showed the appearance of a peak at 6° after soaking, suggesting the intercalation of $C_{60}(Py)^{n+}$ into the film from the edge. These results indicate that the $C_{60}(Py)^{n+}$ intercalation occurred at both the film surfaces and edges, as illustrated in **Fig. S4c**. Defective sites and wrinkles on G-O could also act as “channels” to facilitate the intercalation.

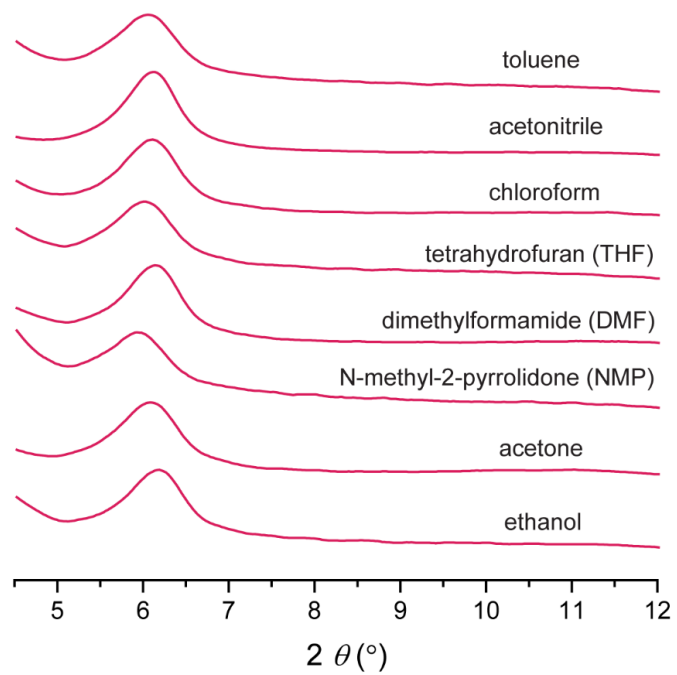


Figure S5. XRD patterns of the [C₆₀(Py)ⁿ⁺]G-O films after 3-day soaking in various organic solvents.

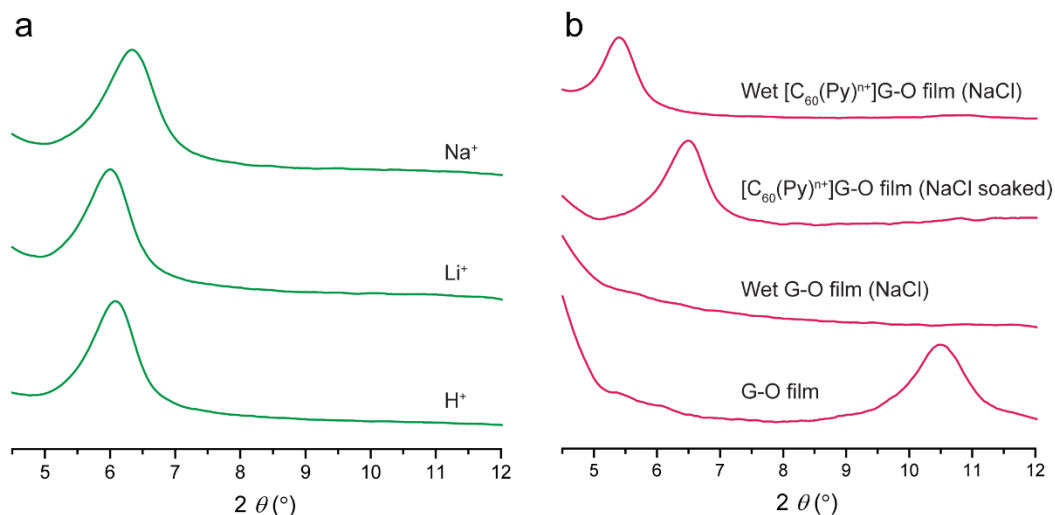


Figure S6. (a) XRD patterns of the [C₆₀(Py)ⁿ⁺]G-O films after 3-day soaking in 0.1 M HCl, LiCl or NaCl. (b) XRD patterns of saline-soaked G-O films and [C₆₀(Py)ⁿ⁺]G-O films.

Monovalent cations could remove multivalent cations from the G-O films by cationic exchange and lead to their disintegration¹. The [C₆₀(Py)ⁿ⁺]G-O film retained its intercalated structure after soaking in 0.1 M HCl, LiCl or NaCl for 3 days (**Fig. S6a**). The slight difference in d-spacing (<0.07 nm) could result from other factors, e.g., humidity and sample batch. The absence of the (001) peak for the saline-wetted G-O film indicates significant swelling (**Fig. S6b**). In contrast, the [C₆₀(Py)ⁿ⁺]G-O film showed a small degree of swelling in saline (0.1 M NaCl), with an increase in d-spacing from 1.4 to 1.6 nm. The stability of the [C₆₀(Py)ⁿ⁺]G-O film against ion exchange suggests a stronger affinity between G-O and C₆₀(Py)ⁿ⁺. In addition, the amount of C₆₀(Py)ⁿ⁺ present in the [C₆₀(Py)ⁿ⁺]G-O film might also influence its stability in a saline solution².

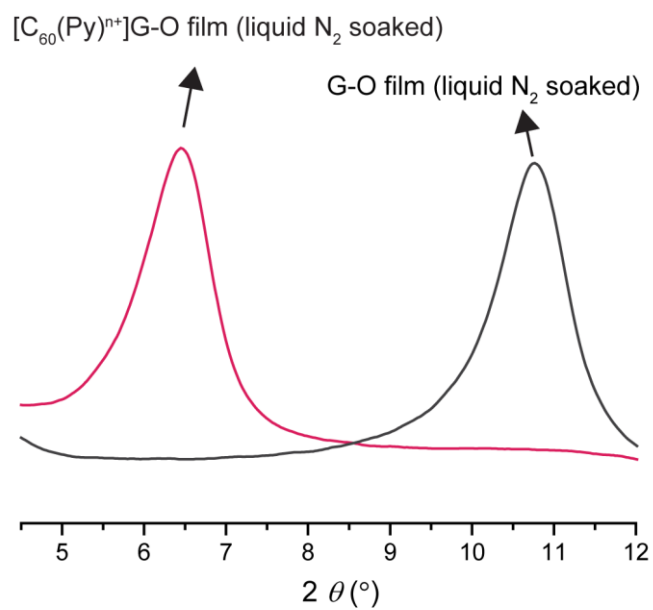


Figure S7. XRD patterns of the G-O film and the [C₆₀(Py)ⁿ⁺]G-O film after “shock cooling” by immersing the films in liquid nitrogen for 1 h prior to thawing in air.

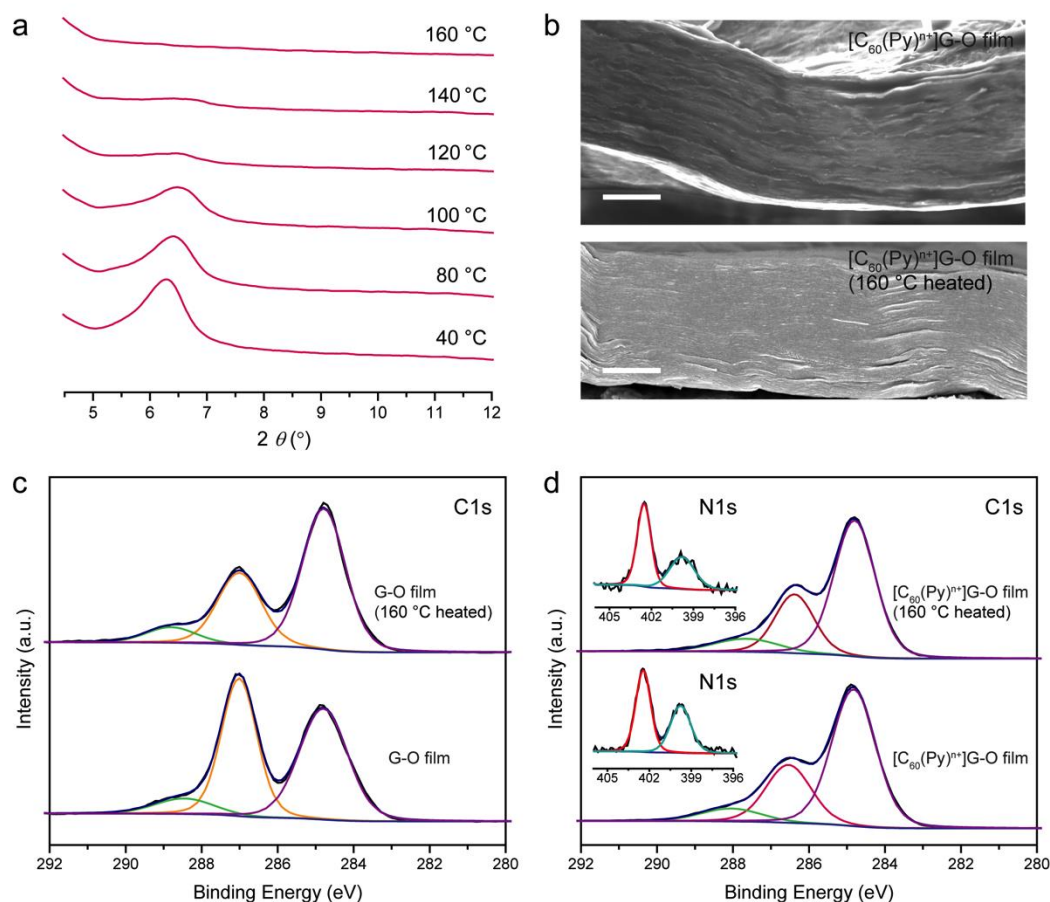


Figure S8. (a) XRD patterns of the $[C_{60}(Py)^{n+}]G-O$ films after heating at different temperatures for 1 h in air. (b) SEM cross-sectional images of the $[C_{60}(Py)^{n+}]G-O$ film before and after heating at 160 °C for 1 h, scale bar, 2 μm . (c, d) XPS C1s and N1s spectra of the G-O and $[C_{60}(Py)^{n+}]G-O$ films before and after 160 °C heating.

The structure of the $[C_{60}(Py)^{n+}]G-O$ film is sensitive to heating, which is indicated by a broadening of the (001) peak as the temperature increased (**Fig. S8a**). The peak disappeared after heating at 160 °C for 1 h. SEM showed little change in thickness after heating (**Fig. S8b**). A decrease in relative intensity of the peak at 287.0 eV in the XPS C1s spectra (**Fig. S8c**) indicates partial removal of oxygen-containing groups from G-O after 160 °C heating. In contrast, the spectrum for the $[C_{60}(Py)^{n+}]G-O$ film remained nearly unchanged after heating to 160 °C. These results suggest that heating leads to restructuring in the $[C_{60}(Py)^{n+}]G-O$ film, possibly caused by the release of gases (**Fig. S20d**), diffusion/clustering of functional groups on G-O and/or redistribution of $C_{60}(Py)^{n+}$ in the film³. The similar XPS N1s spectra (**Fig. S8d**, inset) and the nearly unchanged film thickness indicate that $C_{60}(Py)^{n+}$ was still present in the heated film.

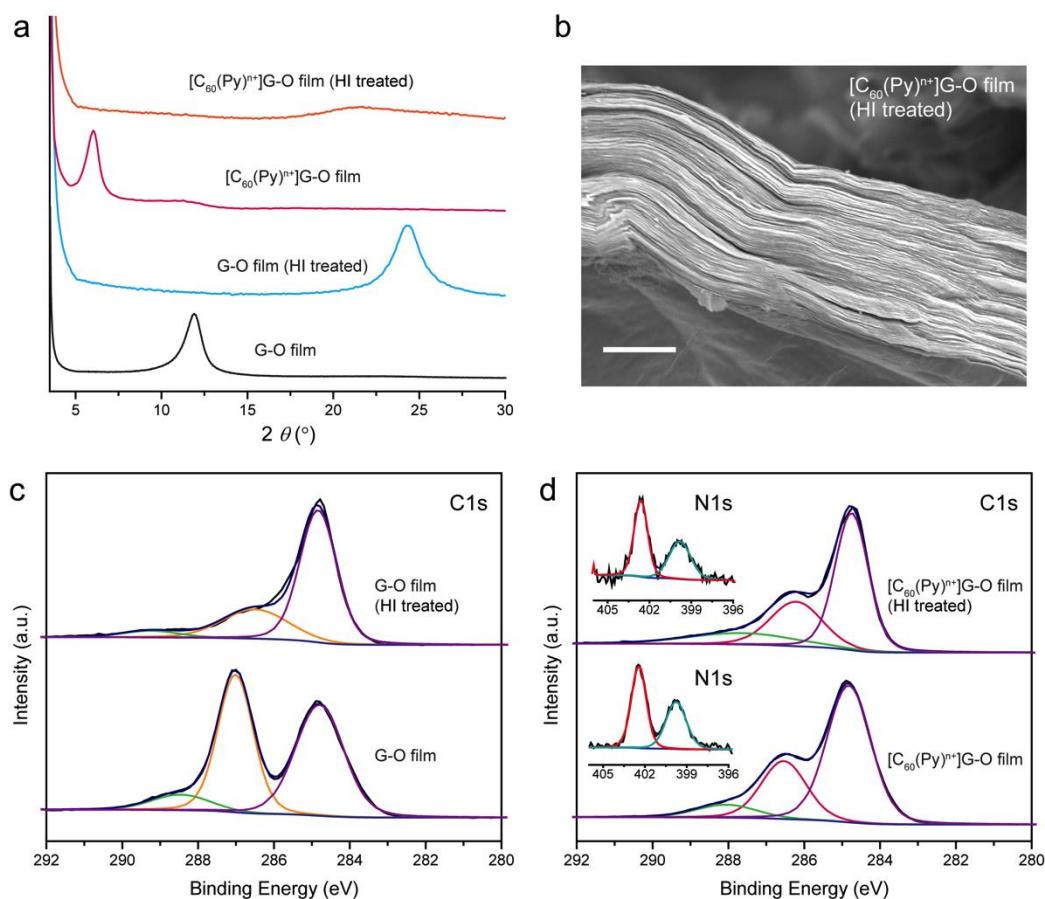


Figure S9. (a) XRD patterns of the G-O and the $[C_{60}(Py)^{n+}]G-O$ films before and after HI treatment. (b) SEM cross-sectional image of the HI-treated $[C_{60}(Py)^{n+}]G-O$ film, scale bar, 2 μm . (c, d) XPS C1s and N1s spectra of the G-O film and the $[C_{60}(Py)^{n+}]G-O$ film before and after HI treatment.

The hydroiodic acid (HI) treatment was carried out following a reported protocol⁴. The G-O or $[C_{60}(Py)^{n+}]G-O$ film was placed inside a glass vial containing 4 mL of HI and 10 mL of acetic acid. The vial was sealed and placed in an oil bath for heating at 40 °C for 24 h. The film was then rinsed with a saturated sodium bicarbonate solution, followed by repeated washing with water and drying in air. The reduction of G-O film led to a shift of (001) peak from 12° to 24° (**Fig. S9a**). In comparison, there was no peak observed for the $[C_{60}(Py)^{n+}]G-O$ film after HI treatment. SEM (**Fig. S9b**) showed that the film retained a compact, layer structure, with a small decrease in film thickness from roughly 4.9 to 4.4 μm after the treatment. A significant removal of oxygen-containing groups is indicated by the apparent decrease in relative intensity of XPS C1s peaks for C-O and C=O groups (**Fig. S9c**). The $[C_{60}(Py)^{n+}]G-O$ film showed a lower degree of deoxygenation, with only a small increase in C/O ratio from 3.7 to 4.2, while, for the G-O film it changed from 2.2 to 6.0. These results suggest that $C_{60}(Py)^{n+}$ might prevent the oxygen-containing groups on G-O from being catalytically transformed and/or substituted by iodide ions. Similar N1s spectra were observed (**Fig. S9d**, inset) for the $[C_{60}(Py)^{n+}]G-O$ film before and after the HI treatment, indicating that $C_{60}(Py)^{n+}$ remained present in the treated film.

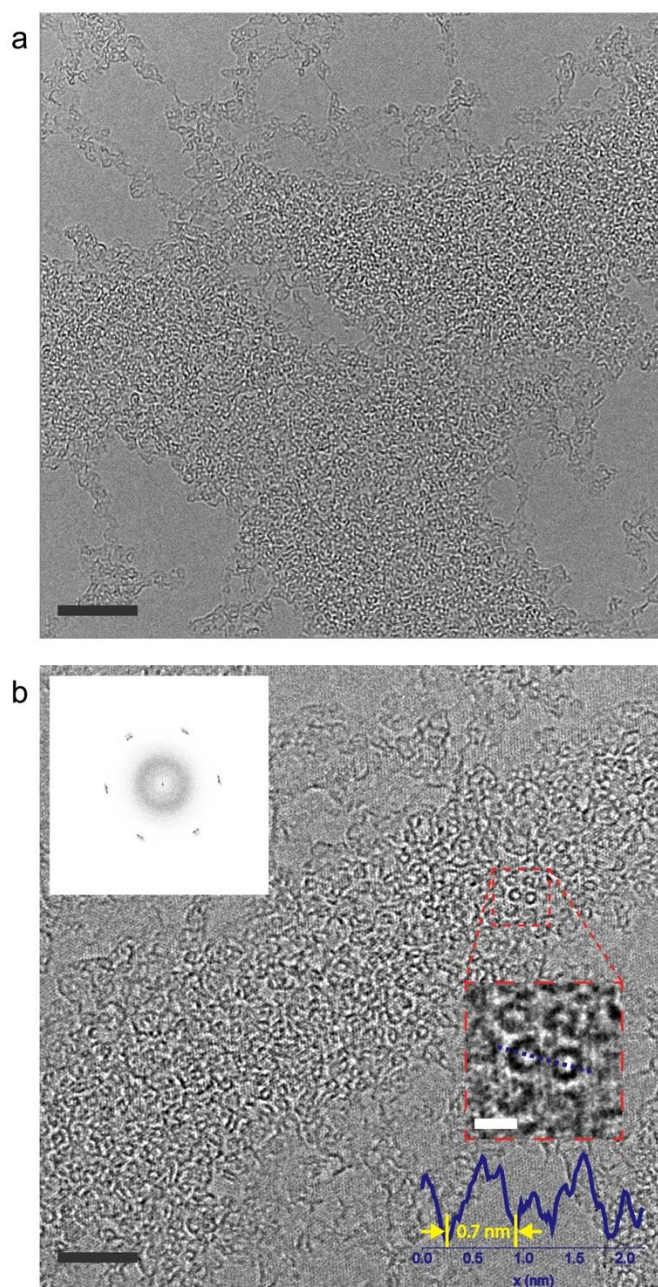


Figure S10. TEM images of the $C_{60}(Py)^{n+}$ salt on a CVD-grown graphene. The inset FFT image from (b) shows a hexagonal pattern from the graphene substrate. The magnified region shows $C_{60}(Py)^{n+}$ molecules, with a plot of the profile along the dotted line indicating 0.7-nm ‘nuclear framework’ diameter of C_{60} . Scale bars, (a) 10 nm; (b) 5 nm; inset, 1 nm.

For HRTEM imaging of the $C_{60}(Py)^{n+}$ salt, a holey carbon-coated, 200-mesh gold TEM grid (SPI Supplies, #3620G-CF) was placed on a CVD-grown graphene-coated copper foil, with the holey carbon film side facing down on the graphene. A drop of isopropyl alcohol was added to the grid to improve the contact of the holey carbon film and graphene. The copper foil was then floated on a 0.1 M ammonium persulfate solution. After etching away the copper, the grid was transferred to the surface of fresh Milli-Q water to remove etchant residues prior to drying in air. A $C_{60}(Py)^{n+}$ salt solution was dropped onto the graphene-coated grid.

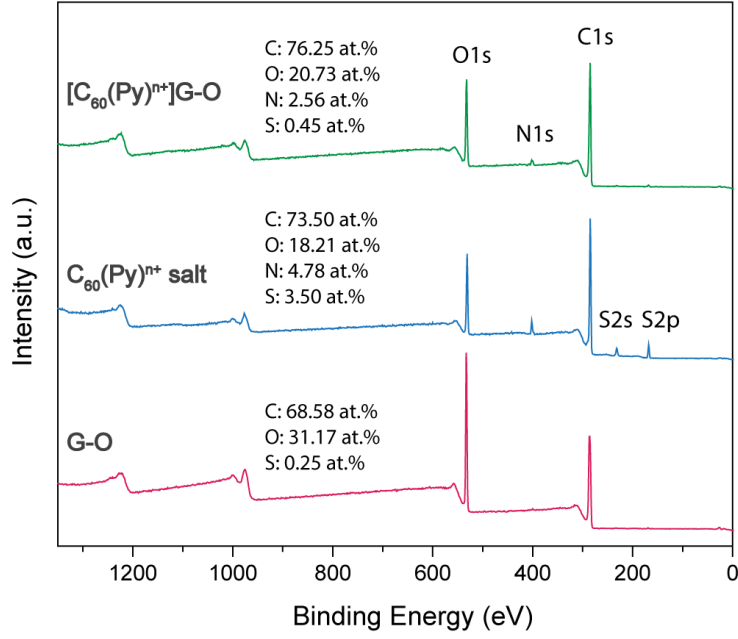


Figure S11. XPS full surveys of the G-O film, the C₆₀(Py)ⁿ⁺ salt, and the [C₆₀(Py)ⁿ⁺]G-O film.

The atomic percentages of C from G-O and C₆₀(Py)ⁿ⁺ in the [C₆₀(Py)ⁿ⁺]G-O film were estimated based on the XPS result. We assume that the atomic ratio of C and N in C₆₀(Py)ⁿ⁺ remained unchanged after intercalation. Since N in the [C₆₀(Py)ⁿ⁺]G-O film is only contributed by C₆₀(Py)ⁿ⁺, the N atomic ratio ('K') can be used to convert the atomic percentage of C from C₆₀(Py)ⁿ⁺ to the equivalent atomic percentage of C from C₆₀(Py)ⁿ⁺ inside the [C₆₀(Py)ⁿ⁺]G-O film ($C_{C_{60}^+ / GO}$),

$$K = \frac{N_{C_{60}^+}}{N_{C_{60}^+ / GO}} = 1.87$$

$$C_{C_{60}^+ / GO} = \frac{C_{C_{60}^+}}{K} = 39.4\%$$

The remaining C is from G-O. To calculate the atomic percentage of C from G-O inside the [C₆₀(Py)ⁿ⁺]G-O film ($C_{C_{60}^+ / GO}$), we have

$$C_{C_{60}^+ / GO} = C_{C_{60}^+ / GO} - C_{C_{60}^+ / GO} = 36.9\%$$

Hence, the percentages of C from G-O and C₆₀(Py)ⁿ⁺ in the [C₆₀(Py)ⁿ⁺]G-O film are 36.9 at.% and 39.4 at.%, respectively.

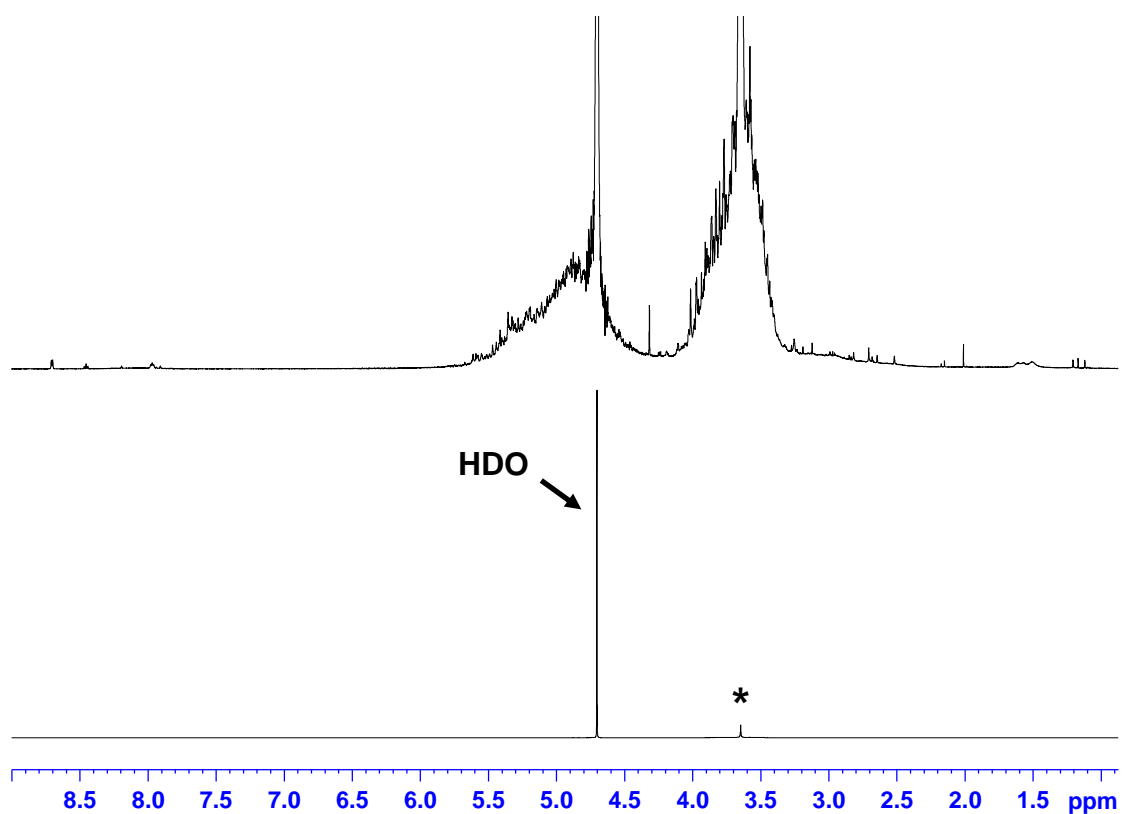


Figure S12. (Bottom) 600 MHz ^1H NMR spectrum at 298 K of the $\text{C}_{60}(\text{Py})^{n+}$ salt 10.5 mg in deuterium oxide 0.65 mL; (Top) 512x expanded view; (*) peak possibly due to methyl sulfate (MeSO_4^-).

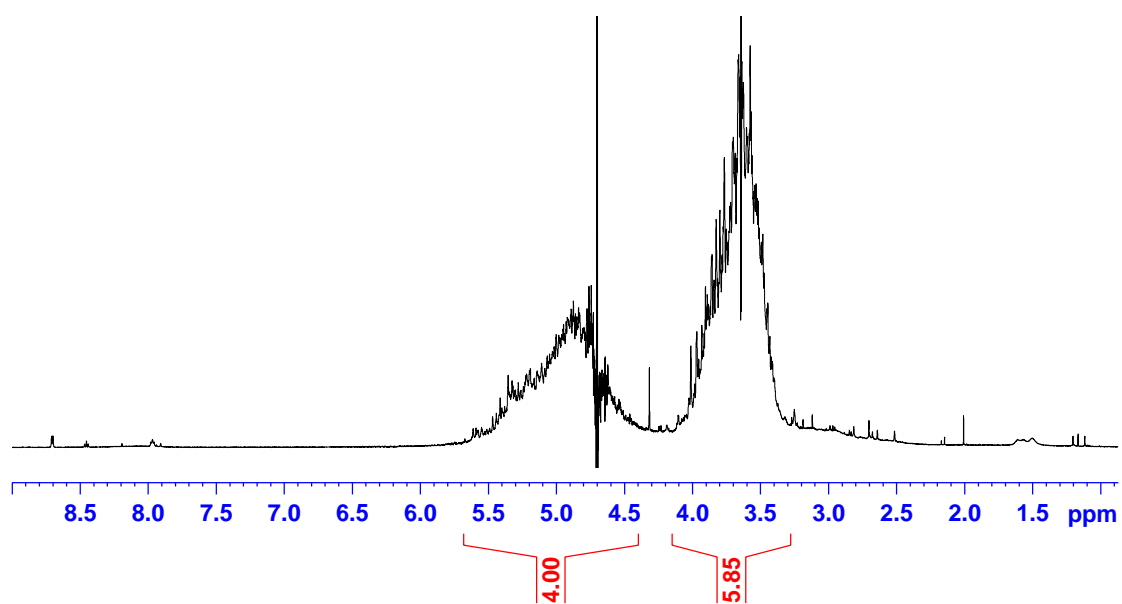


Figure S13. 600 MHz ¹H NMR spectrum at 298 K of the C₆₀(Py)ⁿ⁺ salt 10.5 mg in deuterium oxide 0.65 mL, with the residual water peak at 4.70 ppm and the * peak (**Fig. S12**) possibly for methyl sulfate (MeSO₄⁻) at 3.64 ppm subtracted out.

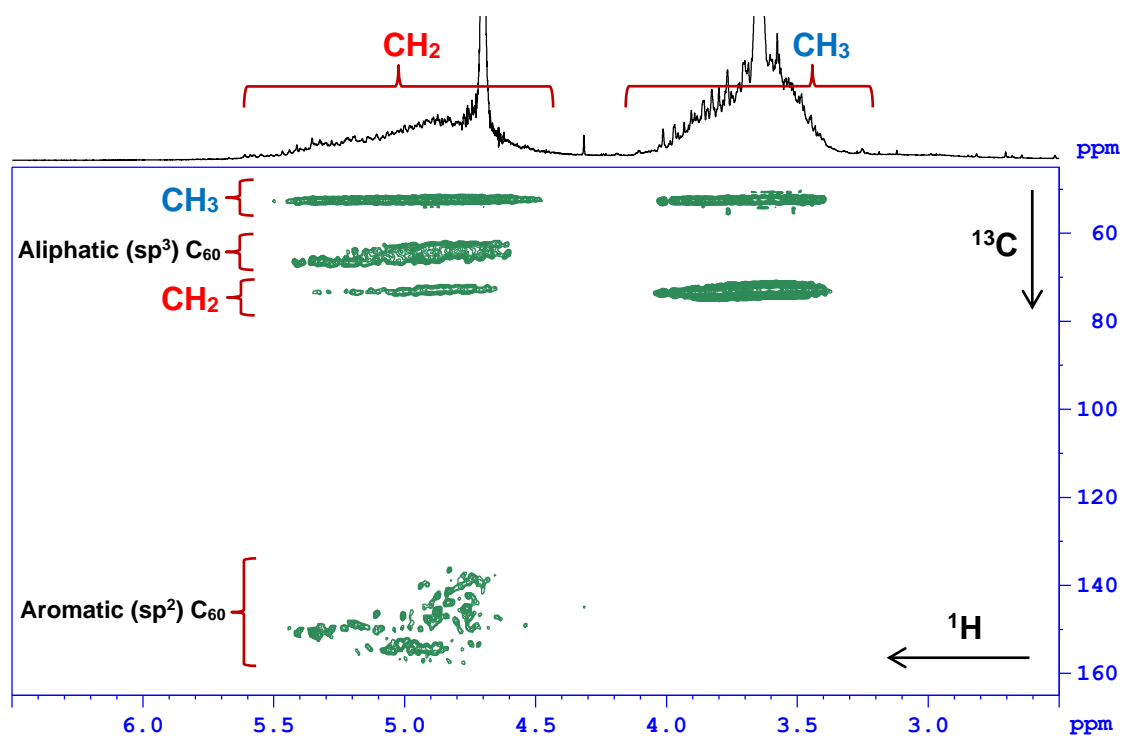


Figure S14. ^1H - ^{13}C HMBC (multiple bond correlation) NMR spectrum at 298 K of 10.5 mg of the $\text{C}_{60}(\text{Py})^{\text{n}+}$ salt in 0.65 mL deuterium oxide, demonstrating connectivity from the CH_3 groups to the CH_2 groups of the **Py** group, and also from the CH_2 to carbons of the C_{60} . Additionally, the CH_3 and CH_2 groups have cross-peaks indicating multiple-bond correlations to themselves, demonstrating the symmetry of the **Py** group.

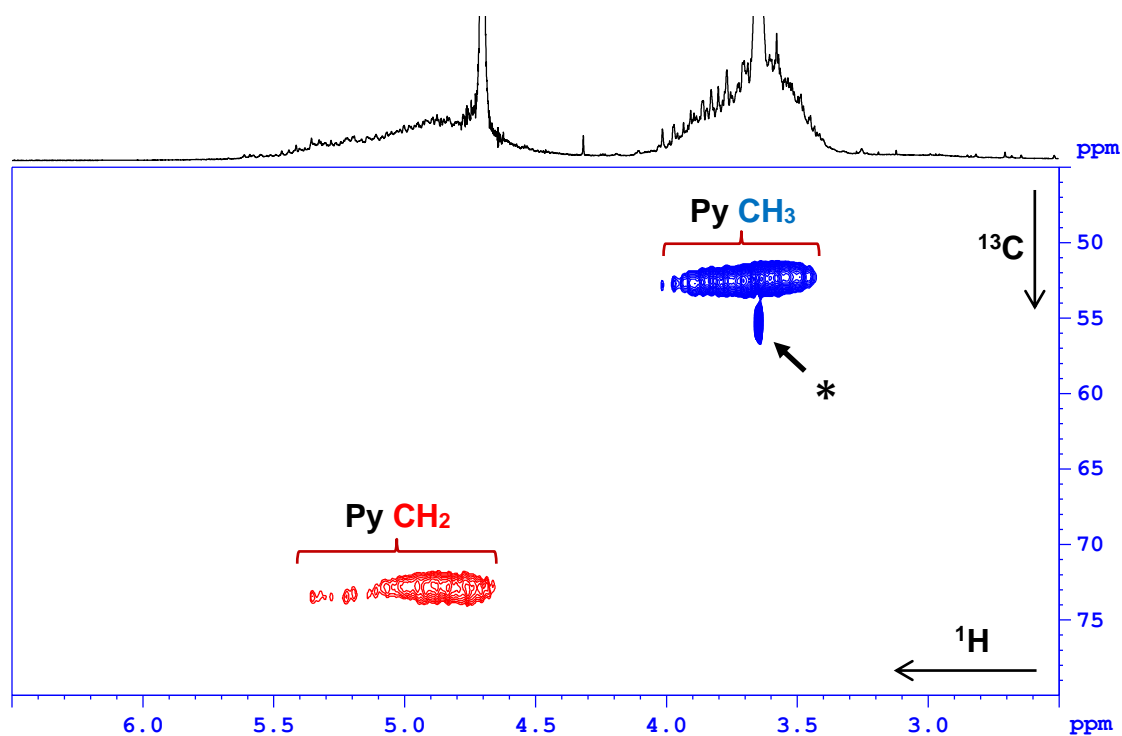


Figure S15. ^1H - ^{13}C HSQC (single bond correlation with multiplicity editing) NMR spectrum at 298 K of 10.5 mg of the $\text{C}_{60}(\text{Py})_n^+$ salt in 0.65 mL deuterium oxide; blue peaks have positive phase, and red peaks have negative phase. The possible methyl sulfate cross-peak (*) in the spectrum, despite its high intensity, has no corresponding cross-peaks in the HMBC spectrum (**Fig. S14**), indicating that it is not part of the $\text{C}_{60}(\text{Py})_n^+$ structure.

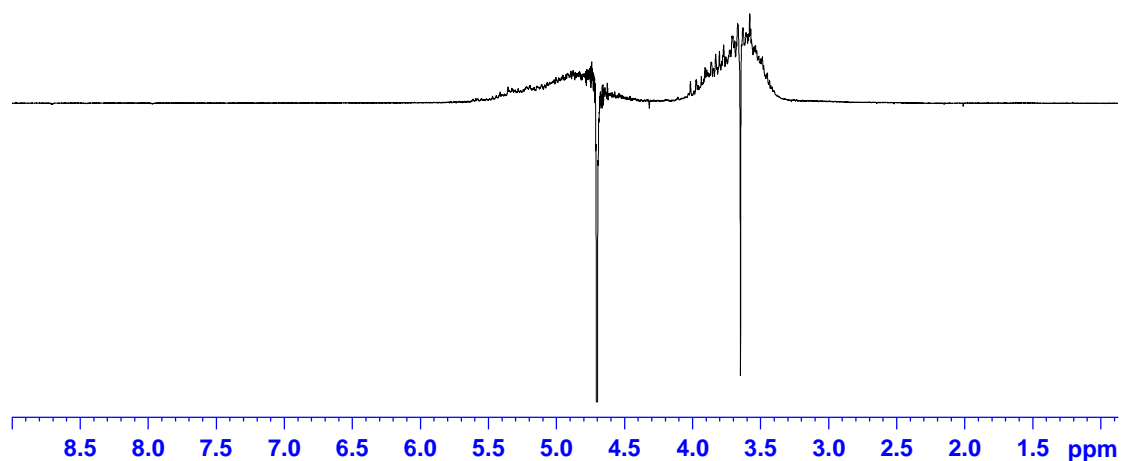


Figure S16. ^1H inversion-recovery NMR spectrum at 298 K of 10.5 mg of the $\text{C}_{60}(\text{Py})^{\text{n}+}$ salt in 0.65 mL deuterium oxide, with d7 delay of 2 s. The CH_3 and CH_2 peaks from **Py** are positive and hence are shown to have significantly shorter T1 relaxation times than water (HDO) at 4.7 ppm and the * peak (**Fig. S12**) at 3.64 ppm, which are still negative. This is consistent with the assignment of a possible methyl sulfate peak, being a small molecule with fast rotational correlation time.

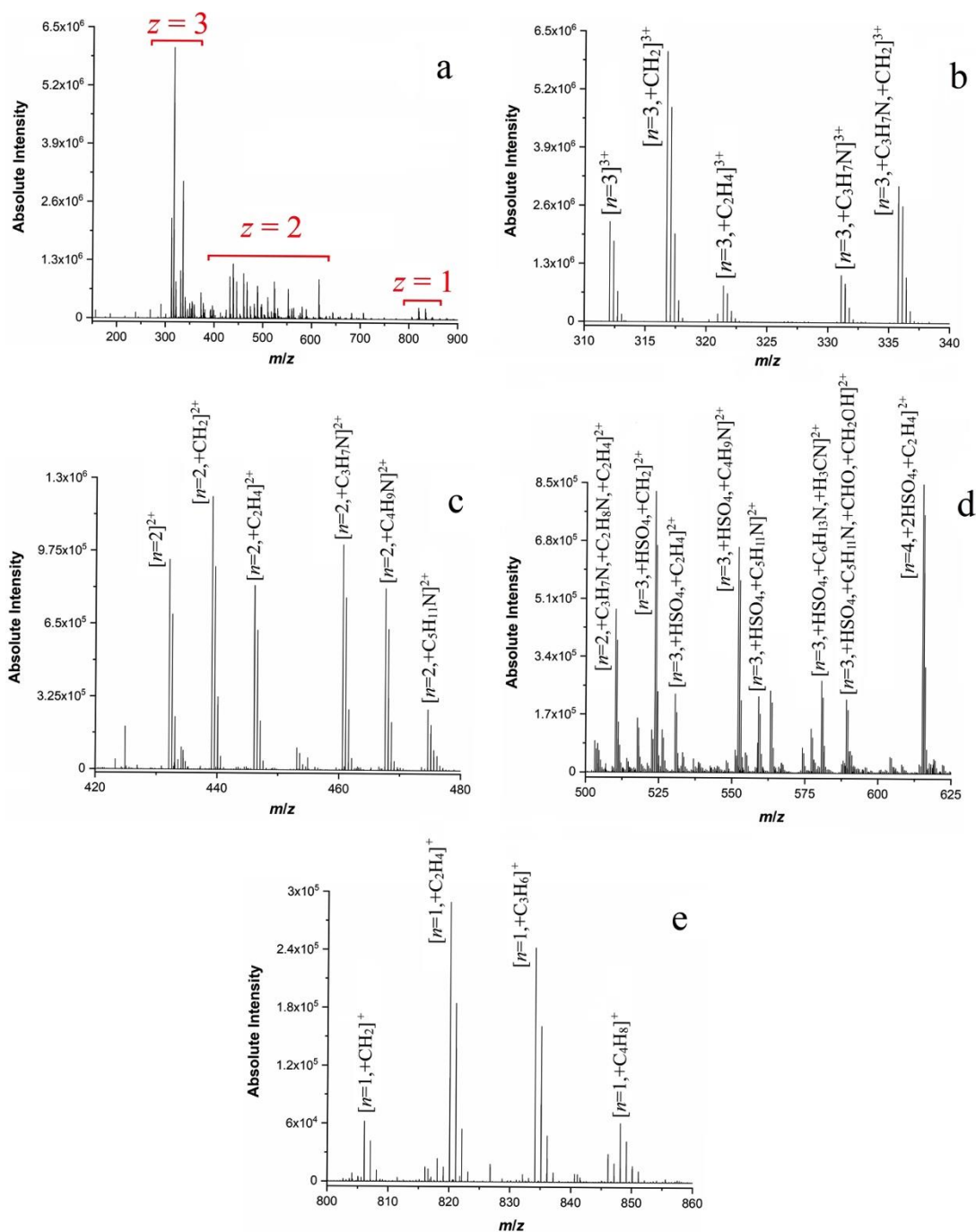


Figure S17. (a) Overall mass spectrum of $\sim 20.0 \mu\text{M}$ $\text{C}_{60}(\text{Py})^{\text{nt}+}$, (b) $z = 3$ region, (c, d) $z = 2$ region, and (e) $z = 1$ region of the mass spectrum.

Table S1. Mass spectrometry results of the C₆₀(Py)ⁿ⁺ molecules.

<i>m/z</i>	<i>n</i>	<i>z</i>	Absolute abundance	Relative abundance	Elemental composition	Mass accuracy (ppm)
615.13366	4	2	8.99E+05	3.95373	[C ₆₀ (C ₄ H ₁₀ N) ₄ +2HSO ₄ +C ₂ H ₄] ²⁺	0.24
312.07901	3	3	2.29E+06	10.07125	[C ₆₀ (C ₄ H ₁₀ N) ₃] ³⁺	0.48
316.75068	3	3	6.05E+06	26.60744	[C ₆₀ (C ₄ H ₁₀ N) ₃ +CH ₂] ³⁺	0.09
321.42224	3	3	8.18E+05	3.59750	[C ₆₀ (C ₄ H ₁₀ N) ₃ +C ₂ H ₄] ³⁺	1.00
331.09797	3	3	1.08E+06	4.74976	[C ₆₀ (C ₄ H ₁₀ N) ₃ +C ₃ H ₇ N] ³⁺	0.16
335.76977	3	3	3.05E+06	13.41367	[C ₆₀ (C ₄ H ₁₀ N) ₃ +C ₃ H ₇ N+CH ₂] ³⁺	0.31
523.60568	3	2	8.32E+05	3.65907	[C ₆₀ (C ₄ H ₁₀ N) ₃ +HSO ₄ +CH ₂] ²⁺	0.26
530.61344	3	2	2.32E+05	1.02032	[C ₆₀ (C ₄ H ₁₀ N) ₃ +HSO ₄ +C ₂ H ₄] ²⁺	0.31
552.13450	3	2	6.76E+05	2.97300	[C ₆₀ (C ₄ H ₁₀ N) ₃ +HSO ₄ +C ₄ H ₉ N] ²⁺	0.11
559.14228	3	2	2.26E+05	0.99393	[C ₆₀ (C ₄ H ₁₀ N) ₃ +HSO ₄ +C ₅ H ₁₁ N] ²⁺	0.12
580.66334	3	2	2.72E+05	1.19624	[C ₆₀ (C ₄ H ₁₀ N) ₃ +HSO ₄ +C ₆ H ₁₃ N+H ₃ CN] ²⁺	0.04
589.15277	3	2	2.22E+05	0.97634	[C ₆₀ (C ₄ H ₁₀ N) ₃ +HSO ₄ +C ₅ H ₁₁ N+CHO+CH ₂ OH] ²⁺	0.08
432.07802	2	2	9.38E+05	4.12525	[C ₆₀ (C ₄ H ₁₀ N) ₂] ²⁺	0.23
439.08573	2	2	1.22E+06	5.36547	[C ₆₀ (C ₄ H ₁₀ N) ₂ +CH ₂] ²⁺	0.38
446.09350	2	2	8.34E+05	3.66787	[C ₆₀ (C ₄ H ₁₀ N) ₂ +C ₂ H ₄] ²⁺	0.41
460.60668	2	2	1.01E+06	4.44190	[C ₆₀ (C ₄ H ₁₀ N) ₂ +C ₃ H ₇ N] ²⁺	0.40
467.61441	2	2	8.14E+05	3.57991	[C ₆₀ (C ₄ H ₁₀ N) ₂ +C ₄ H ₉ N] ²⁺	0.52
474.62225	2	2	2.75E+05	1.20943	[C ₆₀ (C ₄ H ₁₀ N) ₂ +C ₅ H ₁₁ N] ²⁺	0.37
489.13544	2	2	7.43E+05	3.26766	[C ₆₀ (C ₄ H ₁₀ N) ₂ +C ₃ H ₇ N+C ₃ H ₇] ²⁺	2.78
510.15889	2	2	4.85E+05	2.13299	[C ₆₀ (C ₄ H ₁₀ N) ₂ +C ₃ H ₇ N+C ₂ H ₈ N+C ₄ H ₈] ²⁺	0.14
806.09186	1	1	6.36E+04	0.27971	[C ₆₀ C ₄ H ₁₀ N+CH ₂]	0.49
820.10741	1	1	2.98E+05	1.31058	[C ₆₀ C ₄ H ₁₀ N+C ₂ H ₄]	0.46
834.12298	1	1	2.48E+05	1.09069	[C ₆₀ C ₄ H ₁₀ N+C ₃ H ₆]	0.46
848.13854	1	1	6.14E+04	0.27003	[C ₆₀ C ₄ H ₁₀ N+C ₄ H ₈]	0.45

Table S2. Relative amounts of C₆₀(Py)ⁿ⁺ derivatives.

<i>n</i>	Relative amount
4	4
3	66
2	27
1	3

Nanoelectrospray ionisation of ~20 μM C₆₀(Py)ⁿ⁺ resulted in a mass spectrum rich in chemical features containing ions with charge states (*z*) from 1+ to 3+ and C₆₀ functionalised with between *n* = 1 to 4 **Py** groups (**Fig. S17**). The *z* = 3 region of the mass spectrum is shown in **Fig. S17b**. Five major triple charged species with different additions of neutral units were observed. Similarly, the *z* = 2 and 1 regions (**Figs. S17c-e**) show various neutral alkyl additions and HSO₄⁻ adducts. These data and the accurate mass measurements are shown in **Table S1**. Peak assignments for ions with a relative abundance >15%, in terms of their elemental composition and mass accuracy, are also shown in **Table S1**. In general, the measured mass accuracies for all ion assignments were sub-parts per million, which is typically sufficient for the unambiguous assignment of the elemental composition of small molecules. By measuring the relative abundances of the peaks in each region, an approximation of the relative extent of each C₆₀(Py)ⁿ⁺ derivative can be obtained (**Table S2**). Assuming that the ionisation and ion transfer efficiencies are the same for the different ions, the weighted average number of **Py** groups per C₆₀ molecule was calculated to be ~2.7, based on the signal intensities of each derivative.

Method: nESI-MS experiments were performed using an LTQ Orbitrap XL (Thermo Scientific, Waltham, MA). Positive voltages of 0.8–1.2 kV were applied to the nESI emitters in relation to the capillary entrance (200 °C) to the mass spectrometer. nESI emitters with the tip sizes of 0.8-1.0 μm were prepared from borosilicate glass capillaries (Harvard Apparatus, 1.2 mm o.d. 0.68 mm i.d.) using a micropipette puller (Model P-97, Sutter Instruments, Novato, United States). Emitter tips were sputter coated with gold and palladium (Scancoat Six, Edwards, UK). A solution containing ~20.0 μM C₆₀(Py)ⁿ⁺ salt in 49:50:1 (v/v) MeOH:H₂O:HOAc was prepared for analysis.

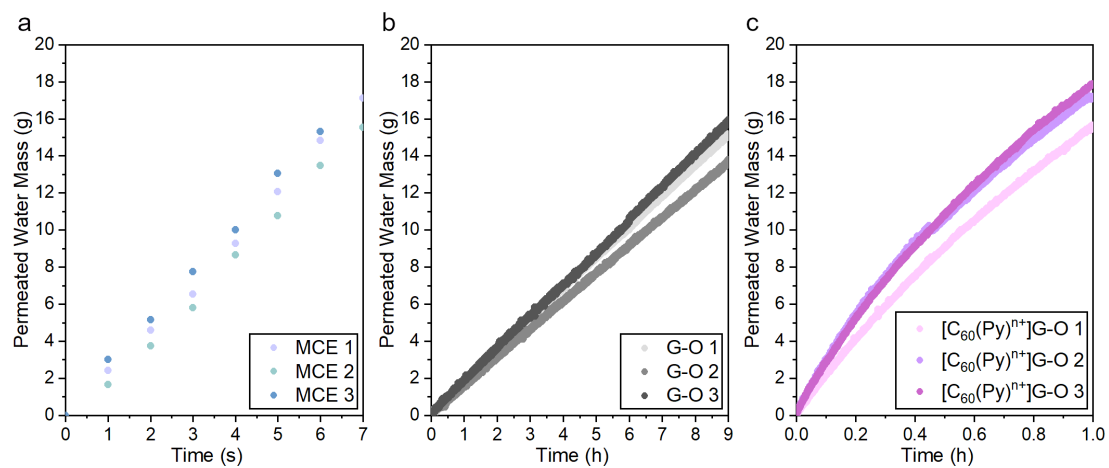


Figure S18. Mass of permeated water recorded at 1 s intervals by mass balance for dead-end filtration for (a) MCE filter, (b) the G-O membrane, and (c) the [C₆₀(Py)ⁿ⁺]G-O membrane.

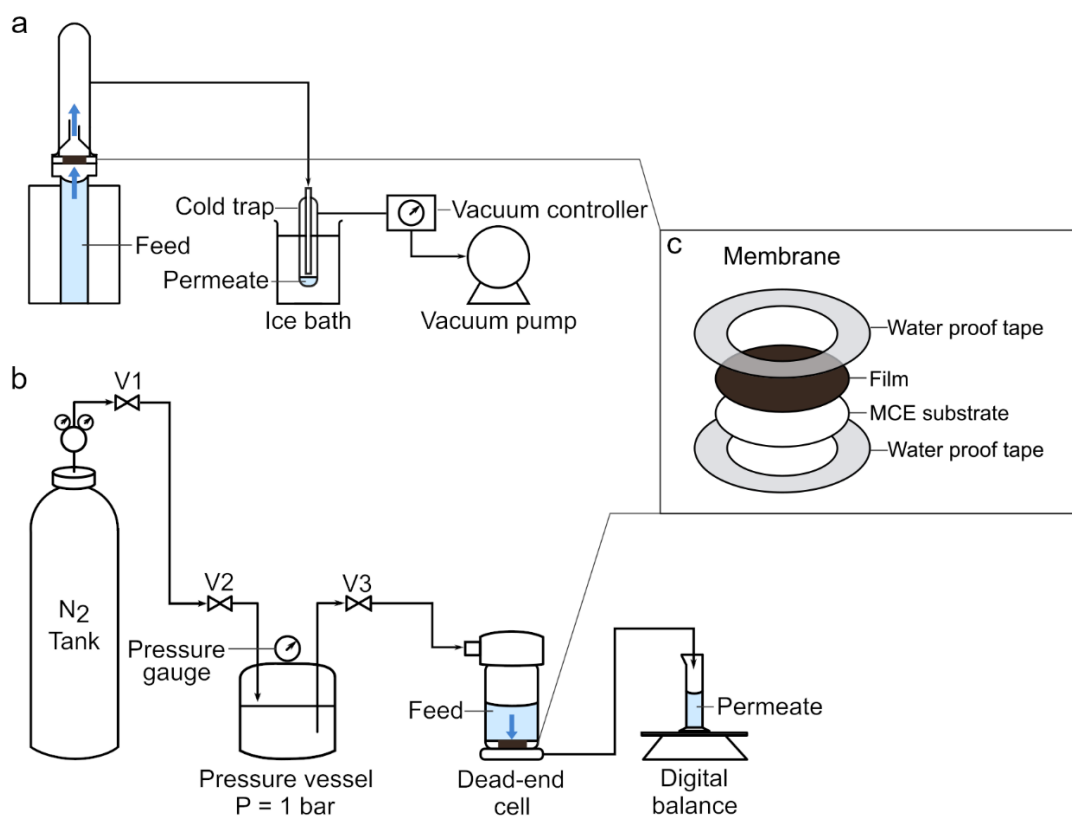


Figure S19. Schematics of (a) vapour permeation and (b) dead-end filtration, with (c) exploded view drawing of the membranes.

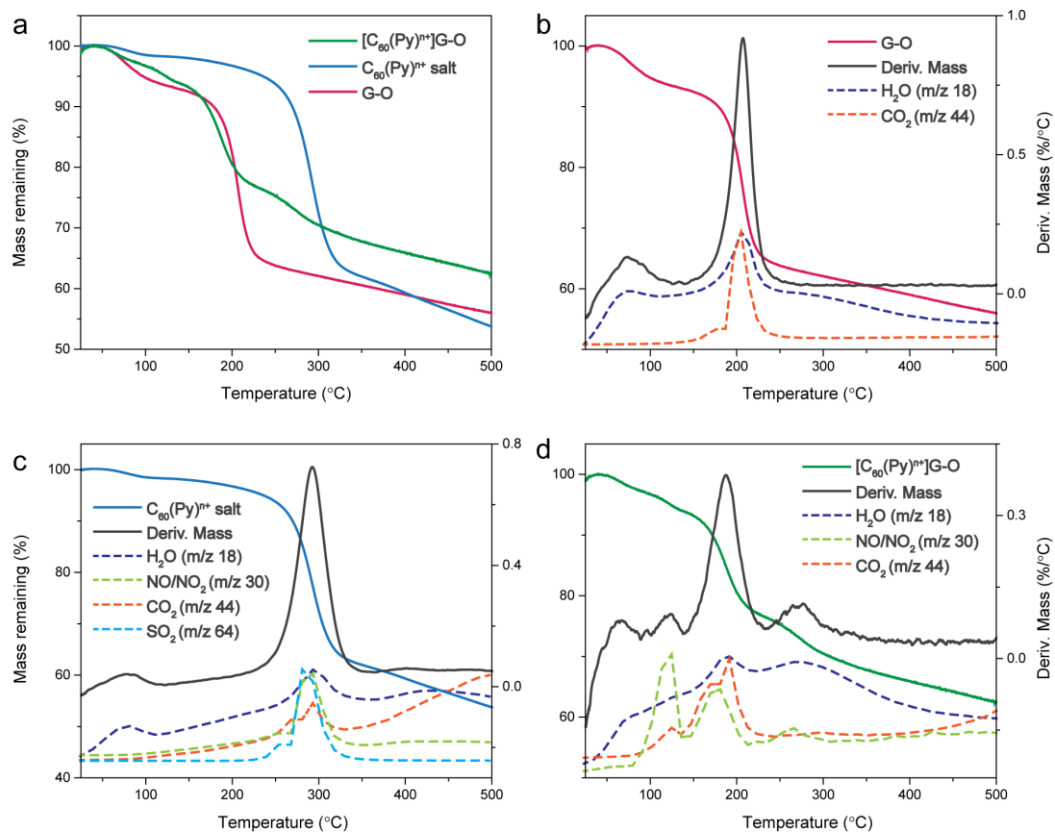


Figure S20. TGA-MS results for the G-O film, the $C_{60}(Py)^{n+}$ salt, and the $[C_{60}(Py)^{n+}]G-O$ film.

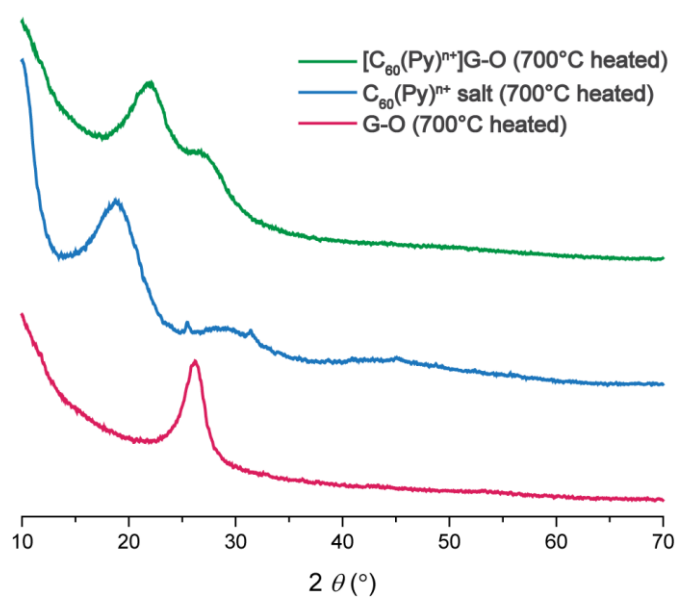


Figure S21. XRD patterns of the G-O film, the $C_{60}(Py)^{n+}$ salt, and the $[C_{60}(Py)^{n+}]G-O$ film after heating to 700 °C.

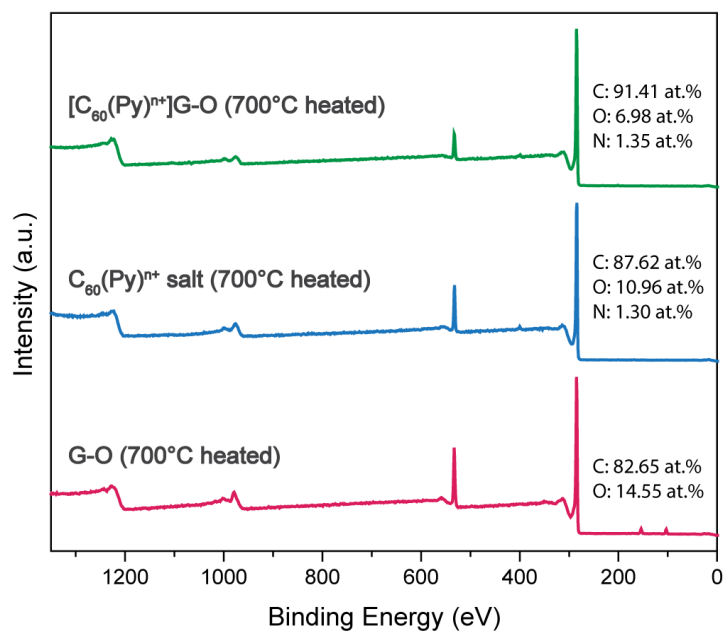


Figure S22. XPS surveys of the G-O film, the C₆₀(Py)ⁿ⁺ salt, and the [C₆₀(Py)ⁿ⁺]G-O film after heating to 700 °C.

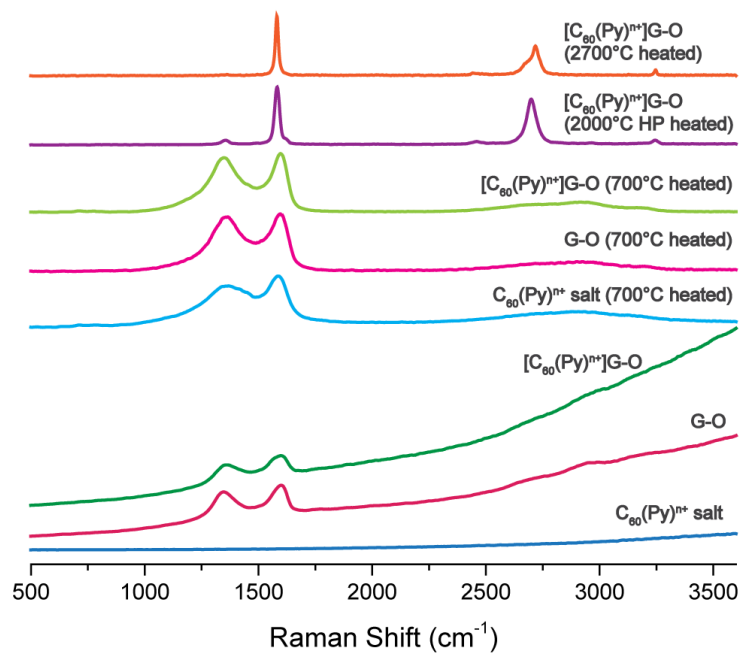


Figure S23. Raman spectra of the G-O film, the C₆₀(Py)ⁿ⁺ salt, and the [C₆₀(Py)ⁿ⁺]G-O film before and after different heat treatments.

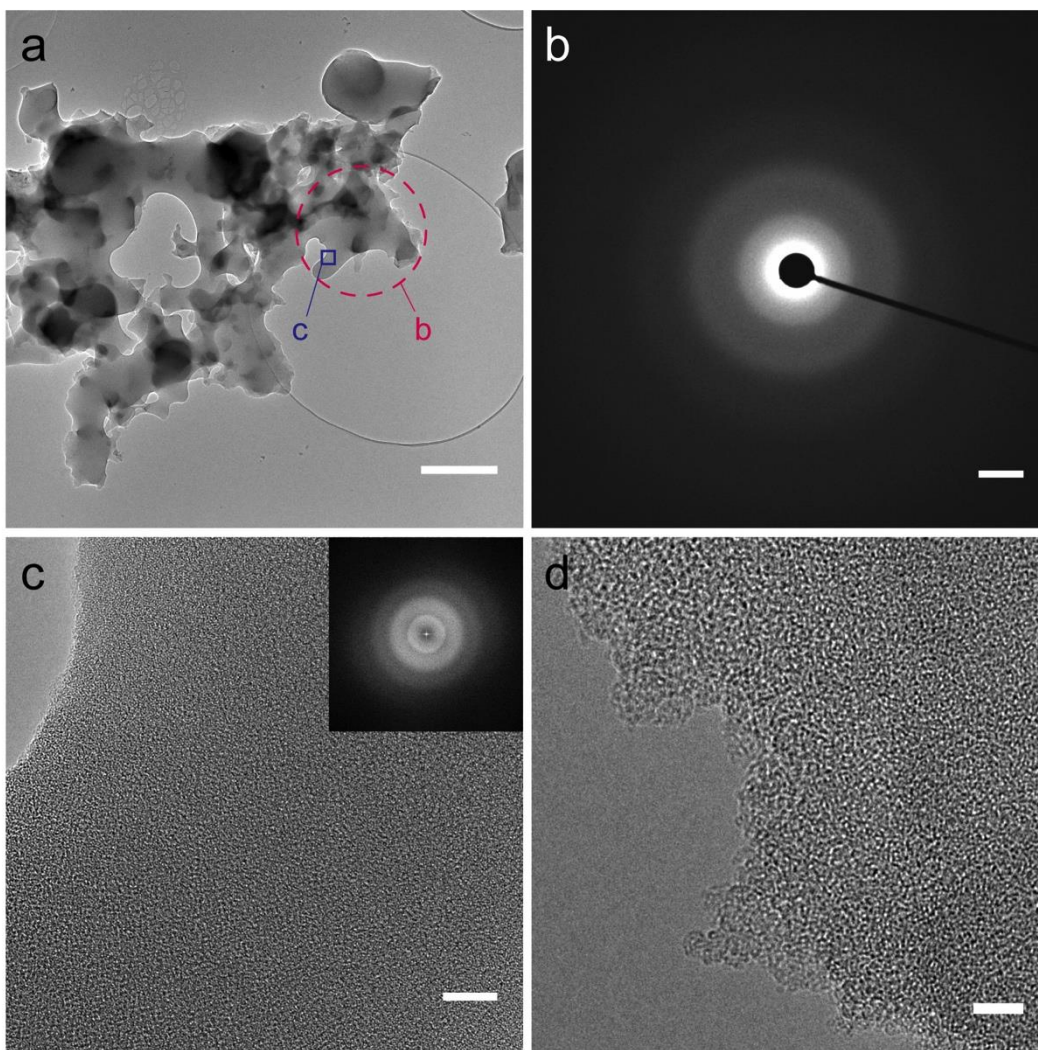


Figure S24. (a) TEM image of residual material after thermal decomposition of the $C_{60}(Py)^{n+}$ salt at 700 °C, scale bar, 500 nm. (b) Electron diffraction pattern from the area indicated in (a). (c) Magnified TEM image from the region indicated in (a), with the corresponding FFT pattern (inset), scale bar, 10 nm. (d) HRTEM image of the residue, showing an amorphous structure featuring highly curved planes, scale bar, 5 nm.

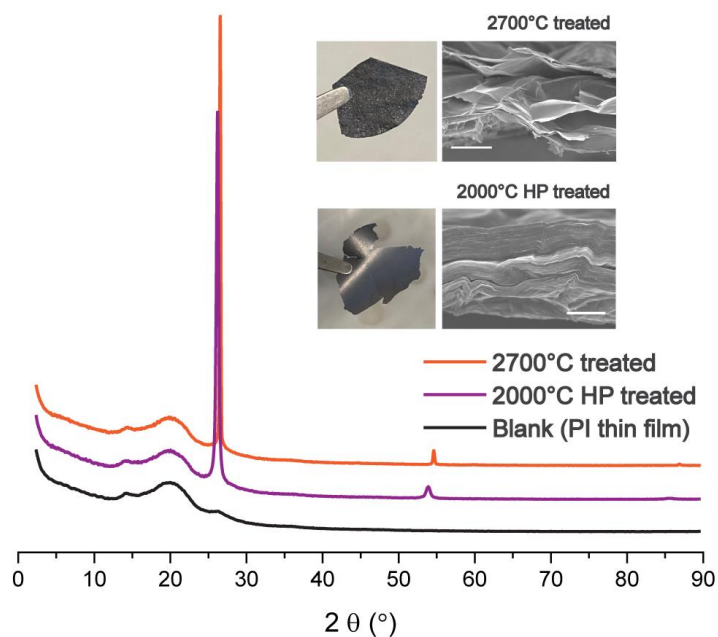


Figure S25. XRD patterns of the $[C_{60}(Py)^{n+}]G-O$ film after hot pressing (HP) at 2000 °C or heating at 2700 °C without physical confinement. Insets are photographs and cross-sectional SEM images of the corresponding films (scale bars, 1 μm , for the 2000 °C HP treated film; 10 μm , for the 2700 °C treated film). The 2000 °C HP treated film retained a smooth surface and compact structure, whereas the 2700 °C heated film expanded and became undulating. The blank is from a polyimide (PI) thin film that was used to confine the sample film during the XRD measurement.

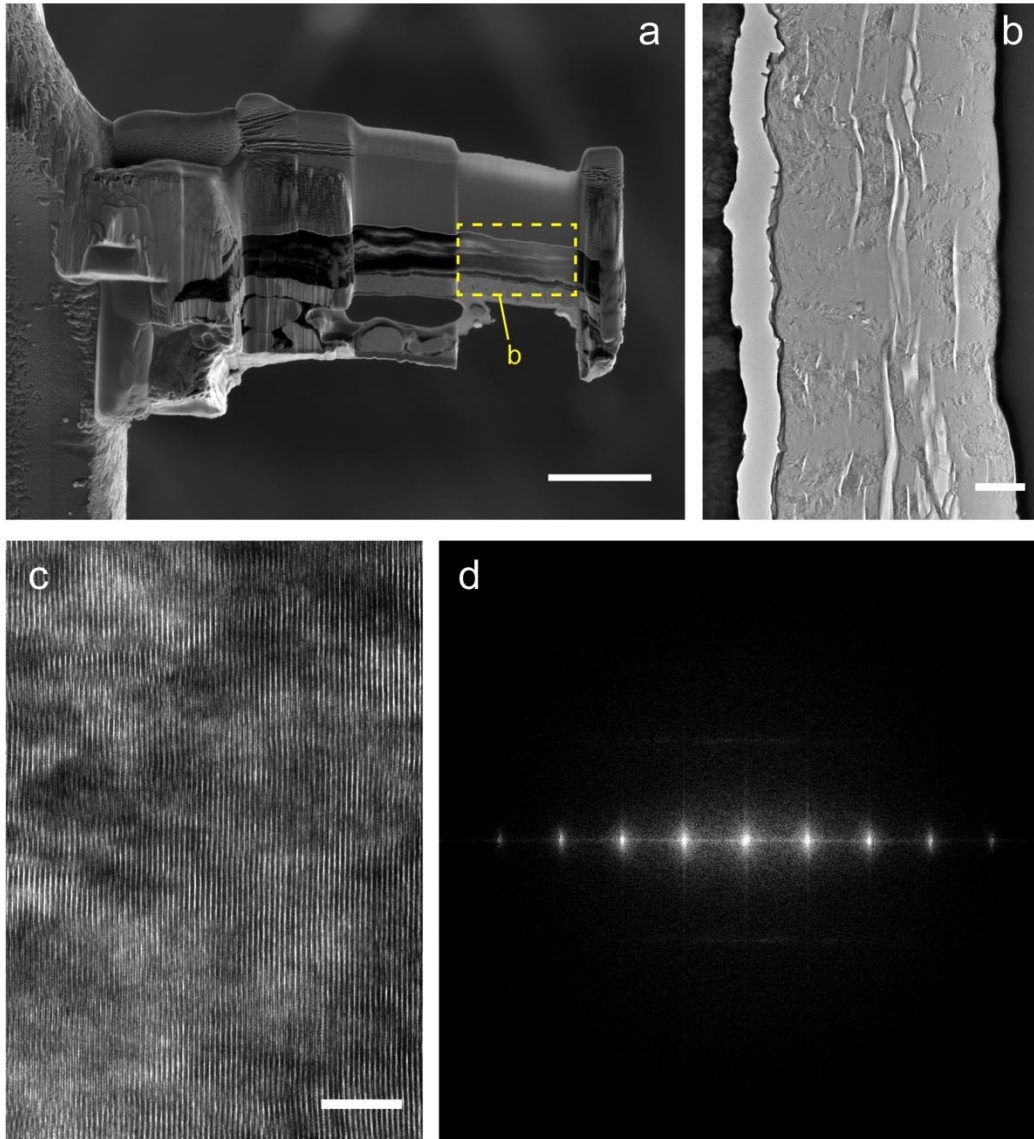


Figure S26. (a) SEM image of FIB-prepared lamella of the 2000 °C HP treated film for TEM analysis, scale bar, 5 μm . (b) Cross-sectional TEM image of the film, scale bar, 500 nm. (c) HRTEM image of the film, showing a parallel arrangement of stacked layers (scale bar: 5 nm), with (d) the corresponding FFT pattern showing parallel layers with a highly graphitised structure.

References

1. Yeh, C. N.; Raidongia, K.; Shao, J.; Yang, Q. H.; Huang, J. On the Origin of the Stability of Graphene Oxide Membranes in Water. *Nature Chem.* **2015**, *7*, 166-170.
2. Yu, W.; Yu, T.; Graham, N. Development of a Stable Cation Modified Graphene Oxide Membrane for Water Treatment. *2D Mater.* **2017**, *4* (4), 045006.
3. Kumar, P. V.; Bardhan, N. M.; Tongay, S.; Wu, J.; Belcher, A. M.; Grossman, J. C. Scalable Enhancement of Graphene Oxide Properties by Thermally Driven Phase Transformation. *Nature Chem.* **2014**, *6*, 151-158.
4. Moon, I. K.; Lee, J.; Ruoff, R. S.; Lee, H. Reduced Graphene Oxide by Chemical Graphitization. *Nature Commun.* **2010**, *1*, 73.